



Cite this: *J. Mater. Chem. A*, 2023, 11,  
12643

# Regulating the electronic structure of single-atom catalysts for electrochemical energy conversion

Wei Ma, <sup>\*a</sup> Zhe Deng,<sup>a</sup> Xinjie Zhang,<sup>a</sup> Zhang Zhang<sup>ab</sup> and Zhen Zhou <sup>\*a</sup>

Single-atom catalysts (SACs) are highly effective in electrochemical energy conversion due to their abundant active sites. Their exceptional electrocatalytic efficiency can be achieved by regulating the electronic structure to optimize the binding energy of intermediates and reduce the energy barrier of electrocatalytic reactions. This is achieved through the metal–support interaction at the interface of SACs. Controlling the electronic structure at the atomic level is a promising strategy for promoting activity, selectivity, and stability. To further understand the influence of electronic structure and accelerate the development of SACs, we summarize various fabrication strategies to construct SACs and further adjust the electronic structure to achieve excellent hydrogen/oxygen evolution and O<sub>2</sub>/N<sub>2</sub>/CO<sub>2</sub> reduction reactions. Finally, we discuss the challenges and prospects of SACs for controllable electrocatalytic processes and provide guidance for the future exploration of electrochemical energy conversion.

Received 9th January 2023  
Accepted 27th February 2023

DOI: 10.1039/d3ta00156c

rsc.li/materials-a

## 10th Anniversary Statement

The *Journal of Materials Chemistry A* is an exceptional platform for sharing findings in the field of materials for energy and sustainability. We have published approximately 50 reviews and research papers since the journal's inception in 2012, including Zhen Zhou, one of the corresponding authors, who serves as an Associate Editor for the journal. Our research focuses on exploring novel materials to address environmental challenges and energy crises. Recently, single-atom catalysts have garnered significant attention due to their remarkable performance and potential in advancing green and sustainable energy. The unique low-coordination environment, quantum size effect, and metal–support interactions of single-atom catalysts make them an exciting avenue of research. In this review, we summarize the recent developments of single-atom catalysts in electrochemical energy conversion. We believe that the integration of advanced preparation methods, *in situ* characterizations, and artificial intelligence will accelerate the development of novel materials, including single-atom catalysts, for energy and environmental applications. We are honored to celebrate the 10th anniversary of the *Journal of Materials Chemistry* and are excited to continue contributing to its growth through the exploration and development of novel energy materials.

## 1 Introduction

The excessive consumption of fossil energy has led to severe environmental issues and energy crises.<sup>1–4</sup> The development and application of clean energy *via* electrocatalytic reactions is a promising strategy for overcoming these hurdles, *i.e.*, splitting water into hydrogen, reducing N<sub>2</sub> into NH<sub>3</sub>, and converting CO<sub>2</sub> into high-value chemicals and fuel cells.<sup>5–10</sup> Single-atom catalysts (SACs) anchored on substrates have been attracting significant attention for increasing the electrocatalytic efficiency resulting from the separated energy levels between the highest occupied and lowest unoccupied molecular orbitals.<sup>11–15</sup> The super-high utilization of active atoms in SACs (almost 100%) reduces the loading of metal elements, especially noble metals, and maximizes active centers.<sup>15–18</sup> SACs optimize the

adsorption/desorption of reaction intermediates to promote the selectivity of products.<sup>19–21</sup> Overall, improved catalytic activity can be achieved by increasing the loading of metal single atoms (SAs) or controlling the carrier to expose a larger surface area to increase the number of active sites, or by modulating the electronic structure and geometry of active sites to increase the intrinsic activity of each active site.<sup>14,22–24</sup> Therefore, SACs can generate higher catalytic activity, selectivity, and stability, and achieve more efficient chemical reactions and energy conversion.<sup>25–29</sup>

Since SACs were first reported in 2011, numerous precious metal SACs, such as Pt, Ir, Ru, and Au, have been obtained through different synthetic strategies, *i.e.*, co-precipitation, impregnation, atomic layer deposition, high-temperature pyrolysis, and low-temperature chemical reduction.<sup>30–49</sup> To further lower the cost of precious metal SACs, 3d transition metal SACs, such as Fe, Co, and Ni, were also fabricated *via* bonding with O, N, S, and P atoms or anchoring at the defects to increase the durability.<sup>50–52</sup> Metal SAs anchored to the substrates interact with each other to generate many active sites.<sup>53,54</sup> The

<sup>a</sup>Interdisciplinary Research Center for Sustainable Energy Science and Engineering (IRC4SE<sup>2</sup>), School of Chemical Engineering, Zhengzhou University, Henan 450001, China. E-mail: mawei@zzu.edu.cn; zhenzhou@zzu.edu.cn

<sup>b</sup>Key Laboratory of Advanced Energy Materials Chemistry (Ministry of Education), College of Chemistry, Nankai University, Tianjin 300071, China



efficiency.<sup>78–80</sup> Although many strategies have been implemented to fabricate/design various SACs and numerous reviews have focused on SACs, few emphasize the influence of the electronic structure on the adsorption/desorption of the intermediates and the electrocatalytic activity.

In this review, first, we briefly summarize the common preparation and characterization methods to fabricate and analyze SACs with different structures (Fig. 1). Then, the influences of the optimized bonding energy, electronic structure, and charge transfer of active sites on the improvement in electrocatalytic activity are discussed. Additionally, we elaborate on recent applications of SACs in electrocatalytic processes including the hydrogen evolution reaction (HER), oxygen evolution reaction (OER), oxygen reduction reaction (ORR), nitrogen reduction reaction (NRR), and CO<sub>2</sub> reduction reaction (CO<sub>2</sub>RR), providing a brief conclusion on the impact of metal SACs in electrocatalytic processes. Finally, we discuss the challenges and prospects of SACs in future electrocatalytic applications.

## 2 Preparation of SACs

SACs are proposed to avoid the agglomeration of isolated metal atoms in the surface of the substrates *via* the confinement or coordination of isolated metal atoms in substrates.<sup>81–83</sup> To date, several fabrication strategies have been employed to prepare SACs by trapping metal SAs at defects or heteroatoms in the substrates to enhance the stability of SACs.<sup>84–86</sup>

### 2.1 Wet chemical methods

The conventional wet chemical method is optimal for fabricating SACs as commercial products due to its easy operation, low cost, and massive production.<sup>87–89</sup> The SACs are fabricated by loading isolated metal atoms on anchored sites.<sup>90–93</sup> The co-precipitation method is performed by adding precipitating agents to aqueous solutions containing various metal cations and adjusting the pH to obtain uniformly dispersed SACs, and the SACs are approached by lowering the loading of metal atoms to prevent aggregation, *e.g.*, Ru<sub>1</sub>/FeO<sub>x</sub> SACs with the low loading of 0.18 wt% was prepared through the co-precipitation method by dissolving ferric nitrate and ruthenium chloride in a NaOH aqueous solution with the pH value of 7.0–8.0.<sup>94</sup> The impregnation method is a traditional route to prepare catalysts by adsorbing metal cations in the solution to the pore channels of the supports.<sup>30,31</sup> The chelation and the viscosity of the solution leach the support and remove the metal element to strengthen the electrostatic adsorption, further dispersing the metal atoms. Therefore, the number of defects greatly influences the loading of metal atoms, and the precise control for SACs is inaccessible.

### 2.2 Atomic layer deposition

Atomic layer deposition (ALD) is a method for depositing the catalysts on the surface of supports at a certain temperature.<sup>95</sup> The deposition process can be precisely controlled by adjusting the number of cycles.<sup>43–45,96</sup> Therefore, the SACs can be

approached by controlling the ALD cycle. Ramesh *et al.* prepared Pt SACs on a porous nitrogen-carbon-powder-coated carbon substrate (NC-CC) by ALD, and the controllable loading of Pt SAs can be approached by adjusting the number of ALD cycles from 2 to 60.<sup>97</sup> However, the high cost and the high-temperature experimental environment would cause the impossibility of large-scale commercial applications.

### 2.3 High-temperature pyrolysis

High-temperature pyrolysis is approached by calcinating the organic precursors, including metal-containing complexes, irregular metal-containing complexes, metal-containing polymers, and a mixture of metal and carbon sources, at 600–1000 °C.<sup>46–48</sup> The isolated metal atoms usually coordinate with the N, S, and P atoms or are trapped by the defects in carbon materials to increase the metal loading and prevent the agglomeration of metal atoms.<sup>49</sup> Therefore, the substrates with numerous defects and heteroatoms provide a promising pathway to fabricating SACs.<sup>98</sup> Al-Zoubi *et al.* used the high-temperature pyrolysis method to prepare non-platinum group metal (non-PGM) electrocatalysts by pyrolyzing a metal-organic framework (MOF) precursor at 750 °C in an ammonia atmosphere.<sup>99</sup>

### 2.4 Low-temperature chemical reduction

Low-temperature chemical reduction is an accessible method for fabricating SACs in a low-temperature environment.<sup>41,42</sup> The precursors containing metal cations frozen in ice are reduced by ultraviolet irradiation or reducing agents (such as NaBH<sub>4</sub>).<sup>100</sup> The size of the metal catalysts can be controlled by adjusting the growth and nucleation process.<sup>101</sup> The Pt SACs were fabricated by irradiating the frozen low-concentration Pt precursor solution with a xenon lamp.<sup>42</sup> Therefore, it was necessary to lower the reaction temperature and the concentration of the precursor solution to fabricate SACs.

### 2.5 Other classical preparation methods

Some classical preparation methods have been adopted to fabricate SACs, *i.e.*, the milling method, microwave-assisted method, and electrochemical method. The preparation of SACs with the milling method relies mainly on mechanochemical forces to create defects in the substrate and capture the atomized metal, in which no other by-products or wastes are generated and the metal loading can be easily tuned by controlling the milling rate. Jeong *et al.* used the milling method to directly atomize the bulk metals onto different supports, such as carbon frameworks, oxides, and nitrides.<sup>102</sup> The microwave-assisted method is considered to be efficient for fabricating SACs within a reduced reaction time. Fei *et al.* rapidly loaded a variety of metal SAs (Co, Ni, or Cu) onto graphene by the microwave-assisted method. The high temperature generated by the microwave heating process allows the N doping and the simultaneous embedding of metal into graphene.<sup>103</sup> Electrochemical deposition is a universal method for the preparation of various SACs, and the SA metal loading can be approached by adjusting the precursor concentration, deposition rate, *etc.* Zeng *et al.* loaded Ir on a Co(OH)<sub>2</sub> substrate

by the oxidation–reduction reaction in the electrolyte and the loading of metal SAs can be precisely adjusted by the concentration of the Ir precursors and the number of scanning cycles.<sup>104</sup>

Although substantial fabrication methods have been implemented to prepare SACs, further fabrication strategies should be developed to generate SACs with high loading, excellent efficiency, and selectivity. The high activity and selectivity of SACs are attributed to the interaction between active atoms and supports, resulting in changes in the electronic structure. Therefore, it is of great significance to study more straightforward and more environmentally-friendly technologies for industrial application.

### 3 Characterizations of SACs

To investigate the morphology and structure of SACs, some characterization techniques have been adopted, including, high-angle annular dark-field scanning transmission electron microscopy (HAADF-STEM), *in situ*-scanning transmission electron microscopy (*in situ*-STEM), scanning tunneling microscopy (STM), X-ray absorption spectroscopy (XAS), Fourier transform-infrared spectroscopy (FT-IR), Raman spectroscopy, and X-ray photoelectron microscopy (XPS). These characterization techniques not only provide local structural information at the atomic scale but also allow further analysis of catalytic mechanisms and structural evolution of isolated atoms and supports, making great significance for studying the reaction mechanism in the electrocatalytic process of SACs.<sup>105,106</sup>

#### 3.1 Electron microscopes

HAADF-STEM was employed to directly observe the dispersed sites in the substrates, which was first applied by Treacy *et al.* in Cavendish Laboratory in 1996.<sup>112</sup> The SACs were detected from the Z-contrast atomic resolution imaging by focusing the electron probe on the specimen and detecting the scattering electrons on an annular dark-field detector.<sup>113,114</sup> HAADF-STEM is considered an efficient technology for observing isolated metal atom bonding in the supports. The uniform contrast of the HAADF-STEM image and energy dispersive X-ray spectroscopy (EDX) in Fig. 2a indicate that single Pt atoms are uniformly distributed on the edge of Ru nanoparticles.<sup>107,115</sup> In recent years, the development of *in situ*-STEM techniques has allowed the observation of dynamic structural changes in SACs. For example, the *in situ*-STEM proved the mobility of Pt SAs dispersed on anatase TiO<sub>2</sub> under different conditions. Pt SAs are located at the original sites under low-temperature oxidation or reduction conditions. However, the reduction conditions (5% H<sub>2</sub>) at 450 °C for 30 min led to the shifting of Pt single atoms and the changing of the lattice fringe of TiO<sub>2</sub>.<sup>108</sup> Additionally, STM was used to image the surface of SACs at the atomic level by the quantum tunneling effect of electrons, and investigate the differences in the electronic properties of the samples caused by the tip current under the applied voltage.<sup>116</sup> The STM image of Fe atoms deposited on GaAs(110) is shown in Fig. 2e, and the Fe atom-induced feature is limited to an area of ~13 Å

in diameter.<sup>109</sup> Several different peaks were observed in the  $dI/dV$  spectra of Fe atoms, indicating that the substitution of Ga by Fe atoms on the GaAs surface resulted in hybridization between the d orbitals of the Fe atoms and the p-like orbitals of the neighboring As atoms (Fig. 2f).

#### 3.2 XAS

XAS includes X-ray absorption near edge spectroscopy (XANES) and extended X-ray absorption fine spectroscopy (EXAFS).

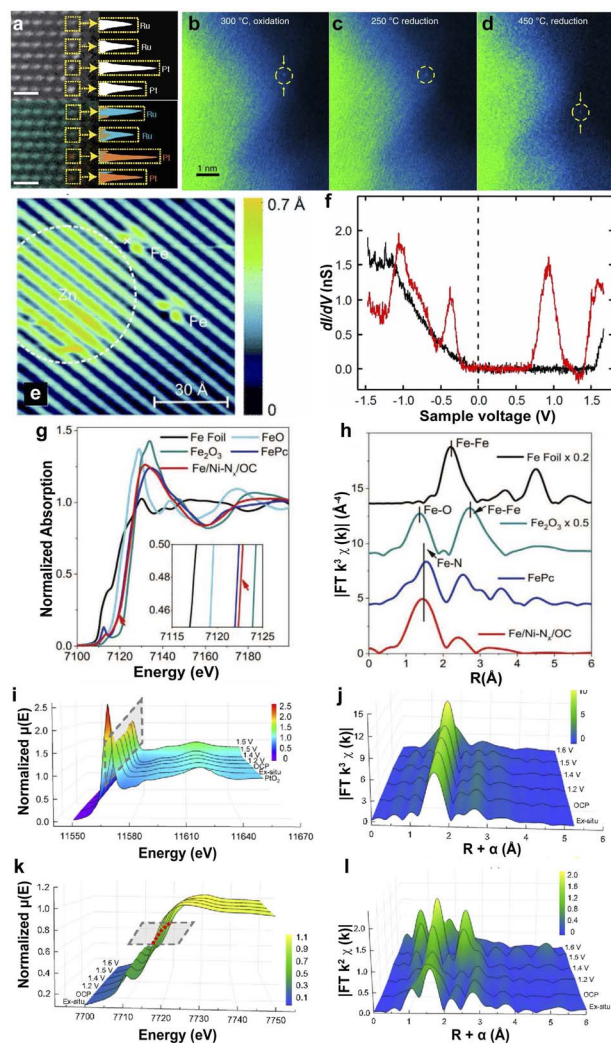


Fig. 2 (a) HAADF-STEM image (top) and EDX map (bottom) of single Pt atoms on a Ru nanoparticle; single Pt atoms (orange), and Ru atoms (blue) are identified in yellow boxes.<sup>107</sup> Copyright 2022, Nature Publishing Group. *In situ*-STEM images of Pt<sub>SA</sub>/TiO<sub>2</sub> under different annealing conditions: 300 °C, O<sub>2</sub> for 30 min (b); 250 °C, 5% H<sub>2</sub> for 30 min (c); 450 °C, 5% H<sub>2</sub> for 30 min (d).<sup>108</sup> Copyright 2019, Nature Publishing Group. (e) STM image of Fe- and Zn-induced structures on GaAs(110). (f) Spectra of  $dI/dV$  as a function of the sample voltage on the clean GaAs(110) surface (black curve) and on the Fe atom-induced structure (red curve).<sup>109</sup> Copyright 2013, American Physical Society. (g) Fe K-edge XANES. (h) EXAFS at the Fe K-edge.<sup>110</sup> Copyright 2020, Wiley. *Operando* potential-dependent XAFS of the XANES (i and k) and EXAFS (j and l) at the Pt L<sub>3</sub>-edge (i and j) and Co K-edge (k and l) of Pt<sub>1</sub>/CoHPO<sub>4</sub>.<sup>111</sup> Copyright 2022, Nature Publishing Group.

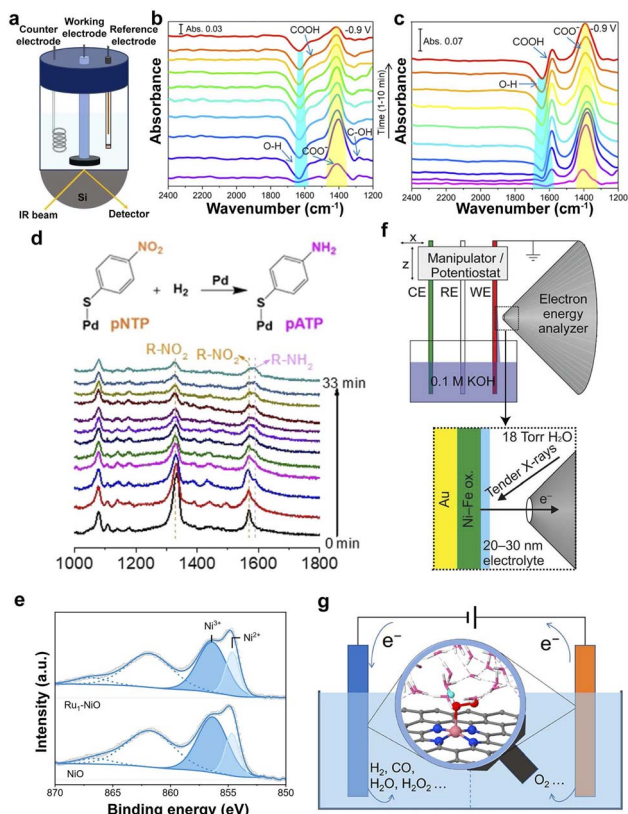


Fig. 3 (a) Schematic illustration of the *in situ* FT-IR configuration for the CO<sub>2</sub>RR. Time-dependent *in situ* IR spectra taken at  $-0.9$  V (vs. RHE) in the CO<sub>2</sub>RR conditions on PdIn@In<sub>2</sub>O<sub>3</sub> (b) and PdIn alloy (c) during the second chronoamperometric test at  $-0.9$  V.<sup>121</sup> Copyright 2022, American Chemical Society. (d) Diagram and *in situ* SERS of the hydrogenation of pNTP over Pd SACs under H<sub>2</sub> at 80 °C.<sup>127</sup> Copyright 2021, Wiley. (e) XPS in the Ni 2p region for NiO and Ru<sub>1</sub>-NiO.<sup>129</sup> Copyright 2022, Wiley. (f) Schematic illustration of an electrochemical cell.<sup>130</sup> Copyright 2016, American Chemical Society. (g) Understanding electrocatalysis at SACs from simulations under realistic electrochemical environments.<sup>135</sup> Copyright 2022, American Chemical Society.

XANES is sensitive to the oxidation state and the coordination environment of SACs, and EXAFS is employed to detect the coordination number, atomic distances, and the species of the neighboring SAs.<sup>117,118</sup> For example, Zhu *et al.* loaded single-atom Fe and Ni sites on hierarchically ordered porous carbon to prepare Fe/Ni-N<sub>x</sub>/OC SACs.<sup>110</sup> The absorption edge position of Fe in Fe/Ni-N<sub>x</sub>/OC is close to that of iron phthalocyanine (FePc), indicating the +2 valence state (Fig. 2g). The similar pre-edge profiles between Fe in Fe/Ni-N<sub>x</sub>/OC and FePc, and the close Fe peak centered in Fe/Ni-N<sub>x</sub>/OC (1.48 Å) to that of FePc (1.50 Å) suggest the formation of Fe-N<sub>x</sub> coordination (Fig. 2h). Furthermore, the SAs with Fe-N<sub>4</sub> coordination were proven by the least-squares EXAFS fitting for Fe/Ni-N<sub>x</sub>/OC SACs. *Operando* XAS is more accurate in identifying active sites and electron transfer under working conditions. The *operando* XAS spectra in Fig. 2i-l suggest the reduced d-band occupancy state of the Co atoms in the CoHPO<sub>4</sub> substrate because of the low oxidation state of Pt and an apparent shift in the absorption threshold of the Co K-edge to higher energies.<sup>111</sup> The electron transfer from

the neighboring Co to Pt and shrinking of the Co-O bond prevent the dissolution of Pt. Similarly, Jiang *et al.* investigated Ni SACs in the CO<sub>2</sub>RR with *in situ* XAS and found no significant changes in Ni XANES under different applied potentials, demonstrating the high stability of Ni SAs in graphene nano-sheets.<sup>119</sup> Therefore, XAS provides a promising method for investigating the interfacial electronic structure and the interaction between metal SAs and supports.

### 3.3 FT-IR

FT-IR is a structural analysis method based on the selective absorption of electromagnetic radiation in the infrared light region, which is employed to probe the local structure, oxidation state, and coordination environment of SACs.<sup>44,120</sup> In particular, *in situ* attenuated total reflectance-Fourier transform infrared (ATR-FTIR) spectroscopy was used to monitor the evolution of COO<sup>-</sup> and COOH intermediates during electrocatalysis (Fig. 3a), proving that the support of In<sub>2</sub>O<sub>3</sub> accelerated the CO<sub>2</sub>RR on the surface of PdIn@In<sub>2</sub>O<sub>3</sub> and CO was the major product along with minor HCOOH (Fig. 3b and c).<sup>120,121</sup>

### 3.4 Raman scattering spectroscopy

Raman scattering spectroscopy is very sensitive to molecular bonding and structure. Therefore, it was employed to characterize the active sites of SACs *via* the fingerprint information of the supports and the change of the species in the solid-liquid interfaces in the low-wavenumber regions, such as oxygen species and hydroxy groups.<sup>122</sup> The surfaces of nanostructured Au, Ag, and Cu can provide enhanced Raman signals, namely, surface-enhanced Raman spectroscopy (SERS), which is more sensitive to trace species on the surface of the catalysts, providing a promising technology for probing the SACs and the reaction mechanisms.<sup>123-126</sup> It was employed to probe the hydrogenation process from *para*-nitrothiophenol (pNTP) to *para*-aminothiophenol (pATP) according to the decreased Raman peak of R-NO<sub>2</sub> and the increased peak of R-NH<sub>2</sub> (Fig. 3d).<sup>127</sup>

### 3.5 XPS

XPS, as a typical surface analysis tool, is used to analyze the elemental composition of the catalyst surface (except H and He elements), the valence information, and the electronic state.<sup>128</sup>

The XPS spectra in Fig. 3e indicate that the loading of single Ru atoms leads to a decreased oxidation state of the Ni in Ru<sub>1</sub>-NiO.<sup>129</sup> The ambient-pressure XPS (APXPS) overcomes the limitation of the vacuum conditions to analyze the changes in the microstructure under the electrochemical reaction conditions by configuring the electrochemical cell (Fig. 3f), proving the initial stages of the oxidation of Ni(OH)<sub>2</sub> to NiOOH.<sup>130-132</sup> Therefore, APXPS is a promising technique for investigating the evolution of the catalysts in the electrocatalytic process.

### 3.6 Computation and simulations

Density functional theory (DFT) computation provides an available method for investigating the adsorption energy

changes in the intermediates on the catalysts and possible reaction processes and helps to screen and optimize SACs.<sup>133</sup> However, the complicated electrocatalysis processes on the solid-liquid interfaces make it difficult to mimic the realistic electrochemical reaction environment because of the sophisticated dynamic electronic charge on the surface and solvation effects. Simulations under realistic electrochemical environments, including solvent and constant-potential effects, can determine the true active site and understand the catalytic mechanism (Fig. 3g).<sup>134–137</sup> Therefore, the computations and simulations provide indispensable guidelines for the rational design of SACs.

The development of various advanced characterization techniques has greatly aided in identifying the structural and electronic properties of active sites on electrocatalysts. However, the breaking of the original chemical bonds and the formation of new chemical bonds on active sites during catalysis will lead to changes in the local coordination environment. Conventional characterization techniques fail to identify the dynamic evolution of active sites, leading to critical process information being missed. Therefore, the development of *in situ* characterization techniques is of great significance for a deeper recognition of active sites and a clearer understanding of catalytic principles.

## 4 Strategies for regulating the electronic structures of SACs

The change in the electronic structure of SACs has a great influence on the adsorption/desorption of the intermediates, thus regulating the electrocatalytic processes and efficiency. Therefore, a suitable electronic structure of SACs is of great significance for accelerating electrocatalysis. To date, there have been some successful strategies for adjusting the electronic structure of SACs *via* central metal atoms, coordination atoms, and metal-support interaction, to improve the electrocatalytic efficiency in different electrocatalytic processes.

### 4.1 Central metal atoms

**4.1.1 Atom-type adjustment.** To investigate the functions of various central metal atoms for the electrocatalytic processes, different SACs of Fe<sub>1</sub>-N-C, Co<sub>1</sub>-N-C, and Ni<sub>1</sub>-N-C were explored for the NRR, proving that Fe with more positive charge prevents the approach of protons and suppresses the HER because of the lower electronegativity, and leads to a higher ammonia yield rate and Faraday efficiency (FE) (Fig. 4a).<sup>138</sup> The interaction between the metal atom and N atoms was further investigated by the projected crystal orbital Hamilton population (pCOHP) by coordinating different transition metals with three different nitrogen-doped carbon structures.<sup>139</sup> The antibonding orbitals in the conduction band (above  $E_F$ ) facilitate the strong adsorption of \*N on Nb@g-C<sub>3</sub>N<sub>4</sub> and Mo@g-C<sub>3</sub>N<sub>4</sub> (Fig. 4b and c). The increased filling of antibonding orbitals leads to a decrease in the strength of the metal SAs bound to \*N from Tc to Ag (Fig. 4d–h). In addition, the integral COHP (ICOHP) by computing the energy integral of the highest

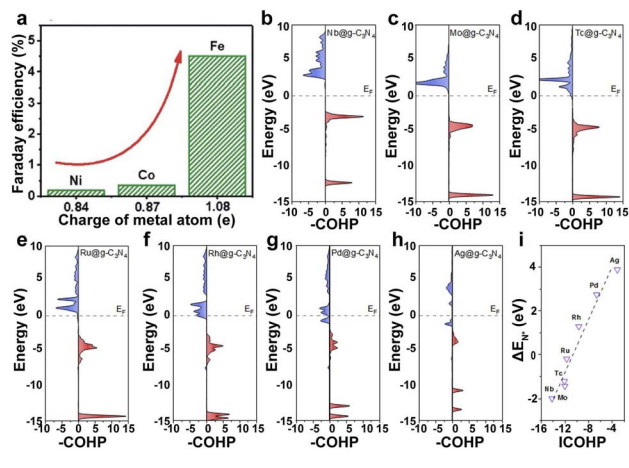


Fig. 4 (a) FE of Fe<sub>1</sub>-N-C, Co<sub>1</sub>-N-C, and Ni<sub>1</sub>-N-C.<sup>138</sup> Copyright 2019, The Royal Society of Chemistry. (b–h) pCOHP between the metal centers from Nb to Ag and the nitrogen atom. (i) Illustration of the correlation between ICOHP and  $\Delta E_{N^*}$ . Red represents bonding contributions, and blue represents antibonding contributions.<sup>139</sup> Copyright 2019, American Chemical Society.

occupied band (below  $E_F$ ) has a linear relationship with  $\Delta E_{N^*}$  (Fig. 4i), suggesting the different activities of the active metal sites on the same support because of the varied adsorption of key intermediates at different metal centers.

**4.1.2 Oxidation state modulation.** In addition to the atom type, the oxidation state of central metal atoms is also important for catalytic reactions.<sup>140</sup> Pt SAs on the defective CeO<sub>2</sub>-Al<sub>2</sub>O<sub>3</sub> support with controlled oxidation states was used to investigate the influence of Pt oxidation states on CO oxidation.<sup>141</sup> Increasing the heat-treatment temperature led to the high content of the metallic state Pt SAs (Pt T, T = 100, 200, 300, 400, 500, and 600 °C) and nanoparticles (NPs). The oxidative Pt SAs showed poorer activity, whereas the metallic Pt SAs presented activity superior to Pt NPs. The highest activity of Pt 300 for CO oxidation was ascribed to the moderate oxidation state and adsorption strength (Fig. 5a and b).

The supports with different heteroatoms accordingly have a great influence on the oxidation state of SAs and electrocatalytic activity.<sup>142</sup> Five kinds of Os SAs with different oxidation states, by modifying the coordination environment of the support, follow the order Os/C < Os/CS < Os/CNS < Os/CN < Os/CS-2 (Fig. 5c), suggesting that the heteroatoms in the supports regulate the oxidation state. The increased oxidation state leads to the decreased occupation of the anti-bonding states of the Os-H bond and further enhances the adsorption of H atoms to Os (Fig. 5d). The low occupancy of the antibonding state around 0 and the increased oxidation state lead to the decreased occupancy of the Os-H bonding states near the Fermi level, decreasing the H\* adsorption intensity (Fig. 5e). Therefore, the HER activities of different Os SACs follow the order Os/CNS > Os/CN > Os/CS > Os/C > Os/CS-2 (Fig. 5f), indicating that the doping of N and S heteroatoms provided an available pathway to regulate the HER activity.

**4.1.3 Strain engineering.** The interactions of neighboring active sites significantly modulate the performance in

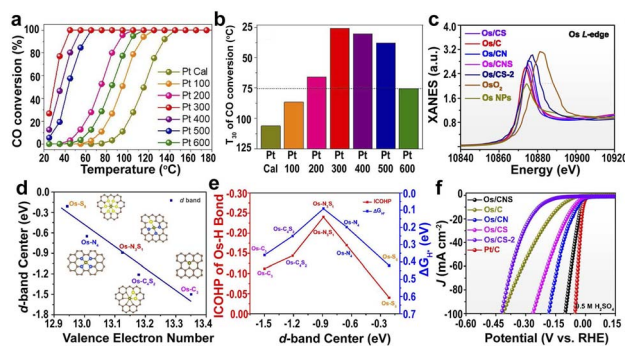


Fig. 5 (a and b) Catalytic activity of Pt SACs (from Pt 100 to Pt 500) and Pt NPs (Pt 600).<sup>141</sup> Copyright 2020, Wiley. (c) XANES of the Os L-edge for different samples. (d) d-band center of the Os single-atom as a function of the valence electron number. (e)  $\Delta G_{H^+}$  and ICOHP of the Os–H bond for H\* on Os SACs as a function of the d-band center of the Os single-atom. (f) HER polarization curves in acidic media.<sup>142</sup> Copyright 2022, Nature Publishing Group.

electrocatalytic processes.<sup>143,144</sup> Atomically dispersed Fe sites with a controllable loading were achieved on nitrogen-doped carbon substrates.<sup>145</sup> The strong interaction between adjacent Fe–N<sub>4</sub> moieties changed the electronic structure and increased the ORR activity because the short inter-site distance ( $d_{\text{site}}$ ) of Fe at the sub-nanometer level increased the d orbital charge density and strengthened the adsorption of hydroxyl intermediates (\*OH) (Fig. 6a). Increasing the distance of adjacent Fe atoms results in a decrease in the intrinsic activity due to the weak interaction and low  $\Delta G_{*OH}$  (Fig. 6b–d), further demonstrating that the electronic interaction of adjacent Fe–N<sub>4</sub> moieties has a significant influence on the ORR process.<sup>11,146</sup>

To further improve the catalytic activity of SACs, the strain effect was approached to mediate the catalytic efficiency by constructing 3D structure modulation on the metal sites. The helical carbon with abundant high curvature surfaces was prepared *via* the carbonization of helical polypyrrole, and the compressive strain was subjected to the Fe–N<sub>4</sub> sites in right-handed helical single atomic iron catalysts (D-Fe SAC).<sup>147</sup> The bending structure and the compressive strain caused the downward shift of the d-band center of the curved Fe–N<sub>4</sub>, weakening the adsorption of intermediates and accelerating the charge transfer between Fe–N<sub>4</sub> sites. Therefore, the D-Fe SAC has a higher ORR activity.

In addition to the SACs, single-atom alloy (SAA) catalysts can enhance the catalytic efficiency because of the tailoring of the electronic structure and synergy effect.<sup>148</sup> The tensile strain induced by Au nuclei in core-shell Au@(PtCo<sub>0.05</sub>)<sub>x</sub> affects the electronic structure of the Co atoms in the Pt lattice.<sup>149</sup> The strong surface tensile strain of Au@Pt<sub>1.5</sub>Co<sub>0.08</sub> caused the positive shift of Pt atoms and the negative shift of Co atoms, resulting in the charge transfer from Co to Pt (Fig. 6e and f), promoting the breakage of O–H bonds and the desorption of OH groups (Fig. 6g). In addition, Au nuclei induced stronger Co–O bonding and promoted H\* desorption, leading to excellent HER activity (Fig. 6h).

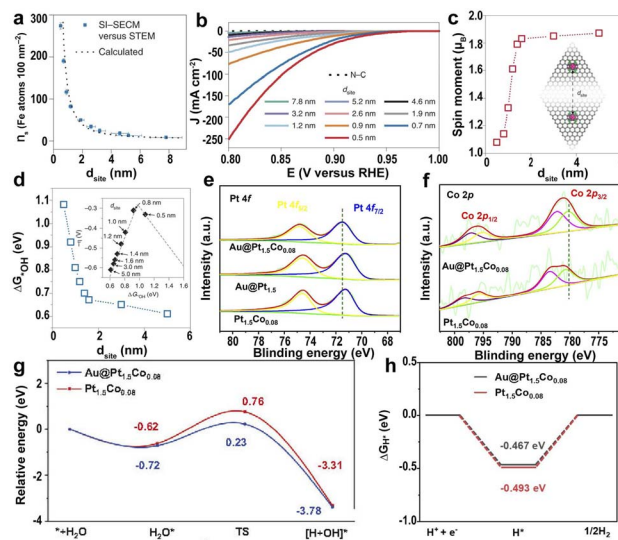


Fig. 6 (a) A plot of Fe atom density ( $n_s$ , Fe atoms per 100 nm<sup>2</sup>) measured with surface interrogation scanning electrochemical microscopy (SI-SECM) vs. the  $d_{\text{site}}$ . (b) Linear sweep voltammetry (LSV) of the PPy-derived N–C and Fe SACs with different  $d_{\text{site}}$  values. (c) DFT-calculated on-site magnetic moments of Fe atoms interacting with neighboring sites with different  $d_{\text{site}}$  values. (d) The  $d_{\text{site}}$ -dependent  $\Delta G_{*OH}$  was obtained by DFT calculations. Inset: volcano plot of calculated overpotentials for the ORR against  $\Delta G_{*OH}$ .<sup>145</sup> Copyright 2021, Nature Publishing Group. High-resolution XPS of (e) Pt 4f and (f) Co 2p for Au@Pt<sub>1.5</sub>Co<sub>0.08</sub>, Au@Pt<sub>1.5</sub>, and Pt<sub>1.5</sub>Co<sub>0.08</sub>. (g) The relative energy diagram along with the water adsorption and dissociation processes on Pt<sub>1.5</sub>Co<sub>0.08</sub> and Au@Pt<sub>1.5</sub>Co<sub>0.08</sub> surfaces. (h)  $\Delta G_{H^+}$  calculated at the equilibrium potential of Au@Pt<sub>1.5</sub>Co<sub>0.08</sub> and Pt<sub>1.5</sub>Co<sub>0.08</sub>.<sup>149</sup> Copyright 2022, Elsevier.

**4.1.4 Heterogeneous metal doping.** The heterogeneous metal atoms in electrocatalysts have a great influence on the electronic structure and the atomic spin state, further adjusting the adsorption energy of the intermediates.<sup>150</sup> The Pt SAs on layered  $\alpha$ -Ni<sub>2/3</sub>Fe<sub>1/3</sub>(OH)<sub>2</sub> generate higher valence and lower coordination conditions of Ni and a more positive charge on Pt, resulting in the favorable adsorption of H\* and OH\* intermediates on Pt and Ni atoms in the hybrid electrocatalyst, accelerating the water-splitting efficiency following the adsorbate evolution mechanism (AEM).<sup>40</sup> However, AEM showed a linear relationship between \*OOH and \*OH ( $\Delta G_{*OOH} = \Delta G_{*OH} + 3.0 \pm 0.2$  eV), resulting in a minimum overpotential of ~0.4 V for the optimal electrocatalysts.<sup>151</sup> To surmount the scaling relation limitation of the AEM, Mo Sas-loaded Ni–Fe oxyhydroxide nanoarrays (Mo<sub>1</sub>–NiFeO<sub>x</sub>H<sub>y</sub>) were used to switch the AEM to lattice oxygen mechanism (LOM) routes.<sup>152</sup> The Mo incorporation leads to a positive shift for Ni and numerous high valence states of Ni<sup>3+</sup> because of the strong electronic interaction in the multimetallic Mo<sub>1</sub>–NiFeO<sub>x</sub>H<sub>y</sub> (Fig. 7a). Mo in Mo<sub>1</sub>–NiFeO<sub>x</sub>H<sub>y</sub> with Mo–O<sub>1</sub> coordination has a low oxidation state and distorted tetrahedral structure (Fig. 7b and c), favoring the charge transfer and lessening the inherent reaction barriers of Mo<sub>1</sub>–NiFeO<sub>x</sub>H<sub>y</sub> in the OER process. Therefore, the high valence state of the active center caused by the Mo atoms leads to the hybridization of metal d and oxygen p orbitals, activating lattice

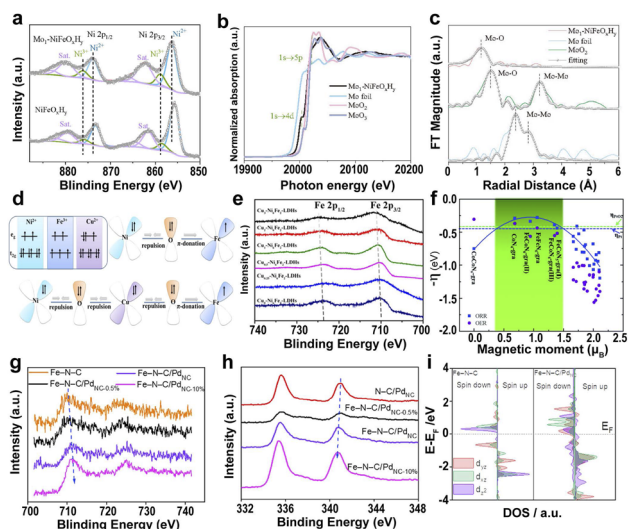


Fig. 7 (a) XPS of Ni 2p for  $\text{Mo}_1\text{-NiFeO}_x\text{H}_y$  and  $\text{NiFeO}_x\text{H}_y$ . (b) XANES of Mo K-edge. (c) EXAFS of Mo K-edge.<sup>152</sup> Copyright 2022, Wiley. (d) Schematics of electronic interactions in the  $d_{xy}$  orbitals of NiFe-LDHs and Cu-NiFe-LDHs. (e) High-resolution XPS scans of Fe 2p.<sup>154</sup> Copyright 2022, American Chemical Society. (f) The negative ORR/OER overpotential as a function of the spin moment on the reaction center atoms. The blue and green dotted lines are the ORR overpotential for commercial Pt and the OER overpotential for  $\text{PtO}_2$ .<sup>155</sup> Copyright 2019, Royal Society of Chemistry. Deconvoluted XPS of Fe 2p (g) and Pd 3d (h) of different catalysts. (i) Projected DOS diagrams of Fe-N-C and Fe-N-C/Pd<sub>NC</sub>.<sup>156</sup> Copyright 2022, Elsevier.

oxygen and leading to excellent OER efficiency.<sup>153</sup> Introducing the heteroatom Cu into NiFe-layered double hydroxides (LDHs) modulates the electronic structure and spin state of Fe.<sup>154</sup> Specifically, the doping of  $\text{Cu}^{2+}$  enhances the  $\pi$ -donation *via* O-Fe-O due to the presence of unpaired electrons of  $\text{Fe}^{3+}$  in the  $d_{xy}$  plane, which makes a higher valence state of Fe element in  $\text{Cu}_x\text{-Ni}_6\text{Fe}_2\text{-LDHs}$  (Fig. 7d and e). Embedding Fe and Co in graphene ( $\text{FeCoN}_x\text{-gra}$ ,  $x = 1-6$ ) leads to a spin magnetic moment of the reaction center, regulates the adsorption/desorption of  $\text{O}_2$ , and increases the ORR/OER activity of the catalyst (Fig. 7f).<sup>155</sup>

Introducing heterogeneous elements to mediate the spin state of the active center atoms also plays a significant role in achieving superior electrocatalytic activity.<sup>157-159</sup> The hybrid electrocatalyst assembled by ultrafine Pd nanoclusters ( $\text{Pd}_{\text{NC}}$ ) and Fe SAs ( $\text{Fe-N-C/Pd}_{\text{NC}}$ ) leads to electron transfer from Fe SAs to  $\text{Pd}_{\text{NC}}$ .<sup>156</sup> The  $\text{Pd}_{\text{NC}}$  induce the redistribution of Fe 3d-orbital electrons and increase the spin state of Fe  $d_{z^2}$  orbitals because of the high electronegativity of Pd (Fig. 7g-i). The high spin state in Fe-N-C/ $\text{Pd}_{\text{NC}}$  creates a wider spin-related channel and promotes the Fe 3d electron spin configuration from low spin to intermediate spin, resulting in high catalytic activity for Fe-N-C/ $\text{Pd}_{\text{NC}}$ . Metal-based SACs loaded on carbon substrates exhibit desirable electrocatalytic activity and good electrochemical stability due to their high electrical conductivity and ability to bind metals.<sup>160</sup> Particularly, two different transition metals Fe and Ni anchored on carbon supports take advantage of the coexistence and the interaction of two different transition metal SAs to modify the coordination environment of the neighboring

atoms, thus improving the ORR performance resulting from the synergetic effects of adjacent Ni-N<sub>4</sub> and Fe-N<sub>4</sub> through the conjugated  $\pi$  bond of graphene.<sup>75,110,161</sup>

## 4.2 Coordination atoms

**4.2.1 Coordination number adjustment.** The coordination number of SACs has a great influence on the electrocatalytic efficiency. The M-NC coordination structure maximizes the utilization of metal atoms and leads to good electrocatalytic performance.<sup>162,163</sup> In particular, most SACs with the square planar M-N<sub>4</sub> configuration were employed to catalyze  $\text{CO}_2$  to CO *via* the electrochemical  $\text{CO}_2\text{RR}$  possess.<sup>164,165</sup> The completely occupied  $3d^{10}$  conformation of Zn severely hinders electron movement. However, low-coordinated Zn atoms in Zn-N<sub>3</sub> or Zn-N<sub>3</sub>-V have an abundant electron environment, resulting in

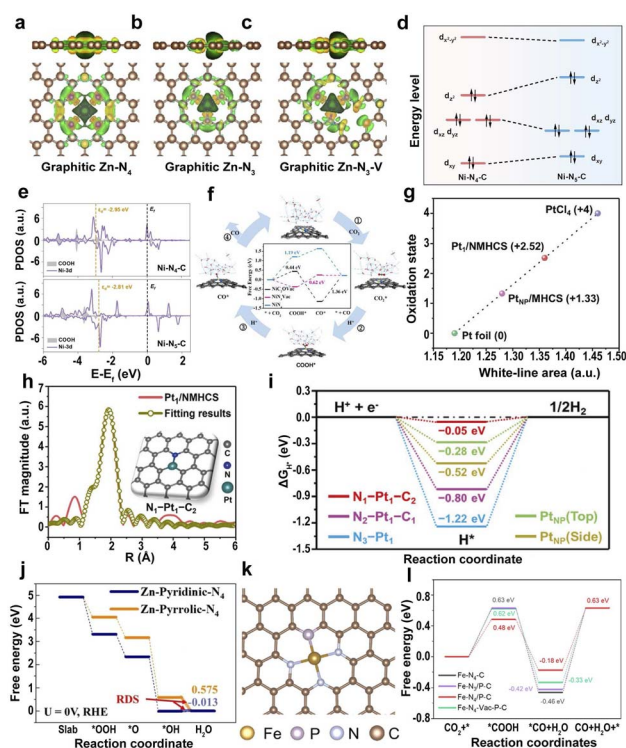


Fig. 8 (a-c) Calculated spatial distribution of charge density for graphitic Zn-N<sub>4</sub>, Zn-N<sub>3</sub>, and Zn-N<sub>3</sub>-V (yellow and green iso-surfaces denote the depletion and gain of electron density, respectively).<sup>166</sup> Copyright 2021, Wiley. (d) Ni 3d orbital splitting of Ni centers on Ni-N<sub>4</sub>-C and Ni-N<sub>5</sub>-C. (e) The d-band center of adsorption structures of \*COOH on Ni-N<sub>4</sub>-C and Ni-N<sub>5</sub>-C.<sup>169</sup> Copyright 2022, Wiley. (f) The proposed reaction pathways and free energy diagrams for the electrochemical reduction of  $\text{CO}_2$  to CO.<sup>170</sup> Copyright 2022, Elsevier. (g) Fitting curve correlating the average oxidation state of Pt of Pt<sub>1</sub>/NMHCS, Pt<sub>NP</sub>/MHCS, Pt foil, and PtCl<sub>4</sub> at the Pt L<sub>3</sub>-edge. (h) EXAFS and the corresponding fitting curve of the Pt<sub>1</sub>/NMHCS. (i) Calculated  $\Delta G_{\text{H}^*}$  values for the HER at the equilibrium potential.<sup>171</sup> Copyright 2021, Wiley. (j) The oxygen-free energy diagrams for Zn-pyridinic-N<sub>4</sub> and Zn-pyrrolic-N<sub>4</sub>.<sup>172</sup> Copyright 2022, Wiley. (k) Atomic structure model of the Fe-N/P-C catalyst. (l) Gibbs free energy profiles of the single-Fe-atom structures with different coordination environments for the electroreduction of  $\text{CO}_2$  to CO.<sup>178</sup> Copyright 2022, American Chemical Society.



a lower valence state of Zn in  $\text{Zn}^{\delta+}\text{-NC}$  and electron transfer from Zn to the adsorbate (Fig. 8a–c), further accelerating the electron movement and promoting catalytic activity.<sup>166</sup> Similarly, two kinds of SACs ( $\text{Co-N}_4$  and  $\text{Co-N}_2$ ) with different N coordination numbers have been prepared by the exfoliation–evaporation strategy.<sup>167</sup> The valence state of Co is lower in  $\text{Co-N}_2$  than in  $\text{Co-N}_4$ , and  $\text{Co-N}_2$  has an asymmetrically distributed electronic structure and more 3d vacant orbitals, which accelerate polysulfide redox kinetics more efficiently than  $\text{Co-N}_4$ . Liang *et al.* prepared Co SACs with different N coordination numbers,  $\text{Co-N}_4$ ,  $\text{Co-N}_3$ , and  $\text{Co-N}_2$  by controlling the pyrolysis temperature.<sup>168</sup> The decrease in the coordination number can increase the electron density of Co SAs and modulate the electron distribution of pyridinic N-bonded C atoms.

The introduction of axially coordinated N atoms into the  $\text{Ni-N}_4$  site to form square-pyramidal  $\text{Ni-N}_5$  leads to a quick increase in the  $d_{z^2}$  orbital energy level of Ni, which facilitates the transfer of electrons from the  $d_{z^2}$  orbital of Ni to the lowest unoccupied molecular orbital of  $\text{CO}_2$ , promoting the adsorption and activation of  $\text{CO}_2$  (Fig. 8d).<sup>169</sup> The d-band center of Ni-3d on  $\text{Ni-N}_5\text{-C}$  with adsorbed  $^*\text{COOH}$  is closer to the Fermi level than that of centrosymmetric  $\text{Ni-N}_4\text{-C}$  (Fig. 8e), leading to the higher adsorption energies of  $^*\text{COOH}$  and lower adsorption energies of  $^*\text{CO}$  on  $\text{Ni-N}_5\text{-C}$ , facilitating the formation and desorption of  $^*\text{COOH}$ . The axial coordination of a nitrogen atom increases the  $d_{z^2}$  orbital energy level and decreases the  $d_{xz/yz}$  orbital energy

level on the  $\text{Ni-N}_5$  active site, increasing the selectivity of the  $\text{CO}_2\text{RR}$  and the limiting step of  $^*\text{CO}_2$  to  $^*\text{COOH}$  and CO desorption. Unsaturated Ni–N species also have a great influence on the efficiency of  $\text{CO}_2\text{RR}$ .<sup>170</sup> The defective  $\text{Ni-N}_3$  structure ( $\text{NiN}_3\text{V}_{\text{ac}}$ ) is considered the active site of Ni-SACs@NC because of the lowest energy barrier for RDS, facilitating the generation of  $\text{COOH}^*$  and increasing the activity of the catalyst (Fig. 8f).

**4.2.2 Coordination atom type adjustment.** To investigate the influence of coordination atoms on the electrocatalytic processes,  $\text{Pt}_1/\text{NMHCS}$  SACs and  $\text{Pt}_{\text{NP}}/\text{MHCS}$  nanoparticle catalysts were fabricated by loading Pt on N-doped mesoporous hollow carbon spheres (NMHCS) and mesoporous hollow carbon spheres (MHCS) with the same loading of Pt.<sup>171</sup> The N in the supports resulted in stronger electron transfer from the single atom  $\text{Pt}_1$  to the NMHCS support because of the high electronegativity of N, enhancing the oxidation state of Pt (Fig. 8g).  $\text{Pt}_1/\text{NMHCS}$  has a unique coordination structure of  $\text{N}_1\text{-Pt}_1\text{-C}_2$ , suggesting that N doping changes the coordination environment of Pt (Fig. 8h). The unique  $\text{N}_1\text{-Pt}_1\text{-C}_2$  structure leads to a low  $\Delta G_{\text{H}^*}$  close to 0 (Fig. 8i), indicating that the  $\text{N}_1\text{-Pt}_1\text{-C}_2$  structure has the highest HER activity. In addition, the  $\Delta G_{\text{H}^*}$  gradually decreased with increasing the amount of N, indicating that the coordination number of N has a significant effect on HER performance because the increased number of N atoms causes electron accumulation on  $\text{N}_x\text{C}_{3-x}$  and significant electron perturbation in  $\text{N}_x\text{-Pt}_1\text{-C}_{3-x}$ .

Different types of coordinated N atoms, such as pyridine N and pyrrole N, have a significant influence on the catalytic performance. For atomically dispersed Zn–N–C SACs, the Zn-pyrrolic- $\text{N}_4$  structure is the origin of high catalytic activity.<sup>172</sup> Specifically, the binding strength of Zn to O with the pyrrole N coordination is lower than that of the pyridine N coordination, leading to the weaker adsorption of oxygen species at Zn sites, thus increasing the intrinsic ORR activity (Fig. 8j). Furthermore, heteroatoms directly coordinated with SAs, such as O, P, S, Cl, and B, can modulate the electronic structure.<sup>173–177</sup> For example, the coordination environment of the Fe site is regulated by introducing P atoms into the Fe–N–C SACs, where the Fe atom co-locates with three N atoms and one P atom (Fig. 8k).<sup>178</sup> The introduction of the P element in Fe–N/P–C SACs reduces the oxidation state of Fe SAs and the formation barrier of  $^*\text{CO}$  intermediates, leading to higher electrocatalytic activity (Fig. 8l). Similarly, Liu *et al.* anchored S to the metal site of Ni SACs, which led to a decrease in the valence state of Ni and promoted the catalytic activity of  $\text{CO}_2\text{RR}$ .<sup>179</sup> Therefore, the adjustment of the coordination atoms has a great influence on the microstructure and the catalytic efficiency.

**4.2.3 Axial ligand coordination modification.** In addition to the conventional coordination atoms (N, S, P, etc.), the intermediates ( $^*\text{CO}$ ,  $^*\text{OH}$ , or  $^*\text{H}$ , etc.) and other atoms can also be axially bonded to metals and modulate the coordination environment of active sites.<sup>137,180</sup> For nitrogen-doped carbon ( $\text{M-N-C}$ ) supporting SACs, the high electronic/structural symmetry of the  $\text{M-N}_4$  site is not conducive to charge transfer during the catalytic process, and axial coordination outside the support plane optimizes the performance of  $\text{M-N-C}$  catalysts.

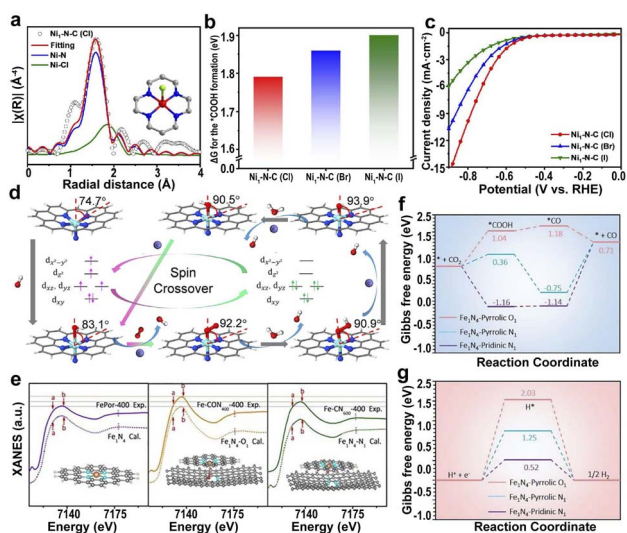


Fig. 9 (a) EXAFS fitting of  $\text{Ni}_1\text{-N-C(Cl)}$ . (b) The  $\Delta G$  for the  $^*\text{COOH}$  formation in  $\text{Ni}_1\text{-N-C(X)}$  catalysts. (c) LSV curves of  $\text{Ni}_1\text{-N-C(X)}$ .<sup>181</sup> Copyright 2022, Springer. (d) Structure and dynamics of the N– $\text{FeN}_4\text{C}_{10}$  moiety in the ORR with optimized geometries (the angles represent the deviation of iron from the  $\text{N}_4$ -plane).<sup>184</sup> Copyright 2020, Elsevier. (e) Experimental XANES curves and the calculated XANES data for  $\text{Fe}_1\text{N}_4$  (FePor–400, by calcinating iron porphyrin at 400 °C),  $\text{Fe}_1\text{N}_4\text{-O}_1$  (Fe– $\text{CON}_{400}$ –400, by calcinating O, N codoped carbon at 400 °C to form  $\text{CON}_{400}$ , and loading iron porphyrin on  $\text{CON}_{400}$  at 400 °C to fabricate Fe– $\text{CON}_{400}$ –400), and  $\text{Fe}_1\text{N}_4\text{-N}_1$  (Fe– $\text{CN}_{600}$ –400, by calcinating O, N codoped carbon at 600 °C under 5%  $\text{H}_2/\text{Ar}$  to form  $\text{CN}_{600}$ , and loading iron porphyrin on  $\text{CN}_{600}$  at 400 °C to fabricate Fe– $\text{CN}_{600}$ –400). Gibbs free energy diagrams for the (f)  $\text{CO}_2\text{RR}$  and (g) HER pathways on Fe sites of different configurations.<sup>185</sup> Copyright 2021, The Royal Society of Chemistry.

The Ni atoms with a high oxidation state coordinated to four in-plane N atoms and one axial halogen atom Cl (Fig. 9a) possess the lowest energy barrier (Fig. 9b) for the RDS (\*COOH formation) in the CO<sub>2</sub>RR process. The strong interaction between Ni in Ni<sub>1</sub>-N-C(Cl) and the \*COOH intermediate and the weak interaction between the single-atom Ni and \*CO lead to the highest electrocatalytic activity for the CO<sub>2</sub>RR (Fig. 9c).<sup>181</sup> Similarly, Liu *et al.* introduced axial phosphate (PO<sub>4</sub>) coordination to improve the OER performance of Co<sub>1</sub>N<sub>4</sub> catalysts.<sup>182</sup> The axial ligand weakens the O-H bond in HPO<sub>4</sub>-Co<sub>1</sub>N<sub>4</sub>, and lowers the energy barrier for dehydrogenation. The axial coordination of Fe-N<sub>4</sub> with the iodine ligand generates reduced 3d orbital energy of Fe and results in weaker adsorption of the key intermediate OH, which would promote OH desorption and thus increase the ORR activity.<sup>183</sup>

Additionally, axial N atoms have a great influence on the spin state of the center atoms, leading to a greater ORR activity of N-FeN<sub>4</sub>C<sub>10</sub> than FeN<sub>4</sub>C<sub>10</sub> (Fig. 9d).<sup>184</sup> The axial Fe-O-coordinated Fe<sub>1</sub>N<sub>4</sub>-O<sub>1</sub> and the axial Fe-N-coordinated Fe<sub>1</sub>N<sub>4</sub>-N<sub>1</sub> are the active sites of the respective Fe SACs (Fig. 9e).<sup>185</sup> The axial O ligand-induced d-band center of the Fe-3d orbital moved to a lower energy level; therefore, Fe<sub>1</sub>N<sub>4</sub>-O<sub>1</sub> has the highest catalytic activity because of the increased CO desorption and inhibitory hydrogen precipitation reactions (Fig. 9f and g).

### 4.3 Electronic metal-support interaction

The strong EMSI between the supports and SACs has a great influence on the electronic structure and catalytic efficiency.<sup>79</sup> The Pt SACs loaded on different transition-metal dichalcogenides (TMDs) lead to different average oxidation states of Pt as follows: Pt-SAs/WS<sub>2</sub> < Pt-SAs/MoS<sub>2</sub> < Pt-SAs/MoSe<sub>2</sub> < Pt-SAs/WSe<sub>2</sub>.<sup>186</sup> However, the acidic HER activity follows the order: Pt-SAs/WS<sub>2</sub> > Pt-SAs/MoS<sub>2</sub> > Pt-SAs/MoSe<sub>2</sub> > Pt-SAs/WSe<sub>2</sub>, suggesting that the high oxidation states of Pt on different supports lead to decreased HER activity (Fig. 10a) because of the narrower d band of Pt SACs resulting from the p-d orbital hybridization between Pt SACs and coordinating atoms (S and Se) (Fig. 10b). The upward-shifted Pd d band leads to more anti-bonding states of hydrogen above the Fermi level, strengthening the affinity of Pt towards hydrogen (Fig. 10c). Therefore, the high oxidation state leads to the strong hydrogen adsorption of the EMSI and poisons the active site because of slow desorption.

In addition to the TMDs, the influence of graphene on the electronic states of SACs was also investigated. A high electron population in the 5d orbitals and a low oxidation state for edge-rich vertical graphene (Pt/VG Ar-5) results in low ΔG<sub>H\*</sub> on the Pt/edge graphene.<sup>187</sup> The d-band center of Pt/VG Ar-5 is closer to the Fermi level because of the strong coupling between the π electrons of the graphene edge and the Pt SACs (Fig. 10d), resulting in excellent HER efficiency for Pt/VG Ar-5. Therefore, changing the location of metal atoms in the support regulates the electronic structure and controls the adsorption energy of the \*H intermediate, accelerating the HER process.

Also, the controllable defects on the transition-metal layered hydroxides with ultra-high surface area and ultra-thin thickness

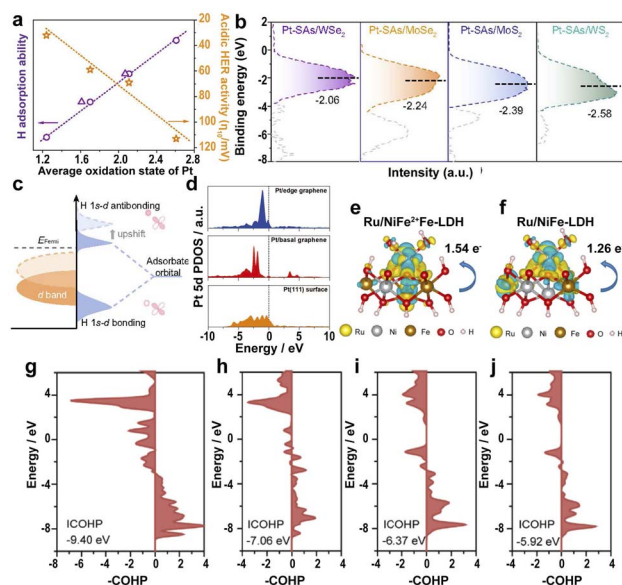


Fig. 10 (a) The relationship between the average oxidation state, H adsorption ability, and acidic HER activity of Pt-SAs/TMDs. (b) Ultra-violet photoelectron spectroscopy–valence band spectra (UPS VBS) of Pt SAs relative to the Fermi level. (c) Schematic DOS diagrams illustrating the EMSI effect on the d-band position of Pt SAs, the interaction between Pt, and chemisorbed atomic hydrogen.<sup>186</sup> Copyright 2021, Nature Publishing Group. (d) Calculated PDOS of the Pt 5d orbital of the Pt/graphene edge, Pt/basal graphene, and a Pt(111) surface.<sup>187</sup> Copyright 2022, Wiley. A comparison of the dissolution of Ru, Ni, and Fe in electrolytes with different charge densities of (e) Ru/NiFe<sup>2+</sup>Fe-LDH and (f) Ru/NiFe-LDH. Yellow and light blue represent the charge accumulation and depletion regions, respectively. pCOHP between the Fe center at the edge near Ru and around the O atom of (g) Ru/NiFe<sup>2+</sup>Fe-LDH, (h) Ru/NiFe-LDH, (i) NiFe<sup>2+</sup>Fe-LDH, and (j) NiFe-LDH.<sup>191</sup> Copyright 2022, Elsevier.

to anchor noble metal SACs allow the fundamental study of the reaction steps and kinetics of the OER.<sup>188,189</sup> Loading Ru atoms on the defective NiFe LDH leads to the electronic transfer from Ru to Ni and Fe, lowering ΔG<sub>H\*</sub> on Ru active sites, and resulting in outstanding HER activity.<sup>190</sup> The strong interaction of SACs reduces the overpotential of RDS for Ru-O, thus accelerating the OER kinetics. However, the active sites tend to form high valence states and dissolve in the electrolyte, leading to serious electrochemical instability. To solve this problem, anchoring Ru SAs on Fe<sup>2+</sup>-doped NiFe LDH (Ru/NiFe<sup>2+</sup>Fe-LDH) leads to the electronic transfer of Fe to high binding energy and Ru to low binding energy in Ru/NiFe<sup>2+</sup>Fe-LDH, lowering the valence of Ru in Ru/NiFe<sup>2+</sup>Fe-LDH, thus improving the electrochemical stability in the OER process.<sup>191</sup> The strong coupling between Ru and Fe<sup>2+</sup> leads to a lower energy barrier of Ru SAs on NiFe<sup>2+</sup>Fe-LDH and lower overpotential on the Fe sites surrounding Ru atoms in NiFe<sup>2+</sup>Fe-LDH, benefiting the electron transfer and facilitating the OER kinetics. More electron transfer between Ru and Fe sites in Ru/NiFe<sup>2+</sup>Fe-LDH than that of Ru/NiFe-LDH resulted in the tight bonding of Ru atoms to NiFe<sup>2+</sup>Fe-LDH, reducing the dissolution of Ru SAs (Fig. 10e and f). The energy-weighted ICOHP value (Fig. 10g–j) suggests that the more negative the ICOHP value, the greater the bond strength.

Therefore, the enhanced Fe–O bond strength in Ru/NiFe<sup>2+</sup>Fe-LDH significantly improves the stability and electrocatalytic efficiency of the catalyst.

Note that the effects of central metal atoms, the coordination environment, and metal–support interactions are integrated into SACs, and cannot be decoupled definitely and studied separately.

## 5 Conclusions and outlook

SACs have been extensively employed in various electrocatalytic reactions, including the HER, OER, ORR, NRR, and CO<sub>2</sub>RR, due to their high electrocatalytic activity and excellent selectivity. The development of electrochemical energy conversion systems is crucial for solving the energy crisis and environmental issues, and SACs hold great promise for advancing these goals. However, the performance of SACs is influenced by several factors, such as electron transfer, metal–support interactions, coordination environment, and the density of the active centers. To further advance the applications of SACs, it is necessary to develop advanced characterization methods that can help us to understand the relationship between the catalyst structure and catalytic activity.

The adjustment of the electronic structure of the active site in SACs mainly uses the following aspects. (1) Metal SAs interactions with supports, namely EMSI, leads to electronic hybridization, charge transfer, and energy transformation between the metal SAs and supports as a perturbation of the electronic structure, including the movement of d band centers and changes in charge distribution. Additionally, the electronic hybridization redistributes charge density between the isolated metal and adjacent atoms and allows the modulation of the adsorption and desorption of reactants, intermediates, and products. (2) Interactions of metal SAs with doping elements. Doping elements such as N and S for carbon supports can change the electronic structure of metal atoms and ultimately enhance the intrinsic activity of active sites. In addition, local defects such as vacancies around metal SAs can be used to adjust the type, number, and position of ligand atoms and thus optimize the adsorption reactants/intermediates/products at the active sites. (3) Interactions between active centers. The low loading of active metal SAs results in a relatively far distance and ignorable interactions between two adjacent active sites. However, in industrial applications, high metal loading is often achieved to pursue lower costs and higher activity. When the distance between two active centers is reduced to the atomic scale, the interaction between active centers will greatly affect the catalytic performance (including catalytic selectivity and efficiency) of the catalyst due to synergistic effects. In addition, in the diatomic system, strong electronic interactions between atoms may lead to a change in the spin state of the active metal atom, affecting the electron transfer path. Whether it is a monoatomic system or a diatomic system with the same or different metals, the synergistic effects between the neighboring metal atoms change the adsorption of the catalytic species, activate the chemical bonds, lower the reaction energy barrier and change the reaction path of intermediates, *etc.*

Accordingly, the hybridization of metal atoms results in more electronic states near the Fermi energy level, improving the electrical conductivity of materials and electron transfer in electrocatalysis, further regulating the charge distribution. The introduction of SAs leads to a dramatic reduction of the energy barrier for the RDS associated with electrochemical reactions.

Despite the rapid development of SACs, there are still many obstacles to overcome in their application. The hindrance of SACs from large-scale industrialization is reflected in high cost, low selectivity, and poor stability. For the practical application of SACs, the development should be accessible in the following aspects.

(1) More advanced characterization techniques. In catalytic processes, the active site often undergoes reversible structural changes due to the interactions with reactants or intermediates, and the structure of active sites often has a decisive influence on the performance. Therefore, advanced characterization techniques are still necessary to precisely identify individual atoms in catalysts, obtain local structural information, and understand the structural evolution of active sites in actual reactions. Additionally, the development and combined use of multiple techniques will play an important role in the development of catalysts. More accurate *in situ/operando* characterizations and computational simulations allow for a more precise understanding of catalytic mechanisms in realistic reaction systems and the targeted design of SACs.

(2) New materials and preparation methods. In electrocatalysis, all metal atoms, coordination atoms, and supports have a great influence on the activity, selectivity, and stability of the catalysts. Different materials interact with each other to produce distinct active sites, and new active species bring more selectivity and possibility to electrocatalysis. However, huge challenges remain in the low loading, uncontrollable coordination environments, and non-uniform distribution of metal sites, leading to poor catalytic performance. Traditional fabrication methods waste resources and time. Machine learning based on databases from high-throughput experiments and computations provides a promising pathway for screening excellent electrocatalysts. In particular, advanced fabrication methods such as 3D printing would promote SACs for practical application.

(3) The introduction of single-atom alloys. Compared with single active sites, the introduction of a second metal atom would improve metal loading and optimize the electronic structure and spin state of metal atoms, providing adsorption sites for multiple reactants and changing the adsorption sites of key intermediates, thus offering the prospect of breaking the possible linear relationship of adsorption energy of the intermediates on SACs. In addition, SAAs can bridge the model and industrial catalysts, and establish clear structure–performance relationships through characterization, computation, and performance evaluations. New knowledge could also be gained about spin or magnetism in electrocatalysis.

(4) Wider applications of SACs. SACs have not been widely applied due to their unclear catalytic processes. To overcome this challenge and enable their industrial use, advanced characterization techniques such as *in situ* and *operando* tools

should be developed. Moreover, SACs with high loading capacity must be achieved for large-scale applications in industry. The development of SACs holds significant potential for important industrial conversion processes, but further research and improvements are needed to enable their wide-spread use.

## Conflicts of interest

There are no conflicts to declare.

## Acknowledgements

This work was supported by the National Natural Science Foundation of China (U21A20281).

## Notes and references

- 1 Y. Ren, C. Yu, X. Tan, H. Huang, Q. Wei and J. Qiu, *Energy Environ. Sci.*, 2021, **14**, 1176–1193.
- 2 Y. Shang, X. Xu, B. Gao, S. Wang and X. Duan, *Chem. Soc. Rev.*, 2021, **50**, 5281–5322.
- 3 G. Wang, J. Chen, Y. Ding, P. Cai, L. Yi, Y. Li, C. Tu, Y. Hou, Z. Wen and L. Dai, *Chem. Soc. Rev.*, 2021, **50**, 4993–5061.
- 4 Y. Xiong, W. Sun, Y. Han, P. Xin, X. Zheng, W. Yan, J. Dong, J. Zhang, D. Wang and Y. Li, *Nano Res.*, 2021, **14**, 2418–2423.
- 5 S. Ding, M. J. Hülsey, J. Pérez-Ramírez and N. Yan, *Joule*, 2019, **3**, 2897–2929.
- 6 P. Liu, Y. Zhao, R. Qin, S. Mo, G. Chen, L. Gu, D. M. Chevrier, P. Zhang, Q. Guo, D. Zang, B. Wu, G. Fu and N. Zheng, *Science*, 2016, **352**, 797–801.
- 7 J. Yang, W. H. Li, S. Tan, K. Xu, Y. Wang, D. Wang and Y. Li, *Angew. Chem., Int. Ed.*, 2021, **60**, 19085–19091.
- 8 J. Liu, M. Jiao, B. Mei, Y. Tong, Y. Li, M. Ruan, P. Song, G. Sun, L. Jiang, Y. Wang, Z. Jiang, L. Gu, Z. Zhou and W. Xu, *Angew. Chem., Int. Ed.*, 2019, **58**, 1163–1167.
- 9 S. Liu, H. B. Yang, S. F. Hung, J. Ding, W. Cai, L. Liu, J. Gao, X. Li, X. Ren, Z. Kuang, Y. Huang, T. Zhang and B. Liu, *Angew. Chem., Int. Ed.*, 2020, **59**, 798–803.
- 10 J. Ge, J. Y. Zheng, J. Zhang, S. Jiang, L. Zhang, H. Wan, L. Wang, W. Ma, Z. Zhou and R. Ma, *J. Mater. Chem. A*, 2021, **9**, 14432–14443.
- 11 A. Kulkarni, S. Siahrostami, A. Patel and J. K. Nørskov, *Chem. Rev.*, 2018, **118**, 2302–2312.
- 12 T. Cui, Y.-P. Wang, T. Ye, J. Wu, Z. Chen, J. Li, Y. Lei, D. Wang and Y. Li, *Angew. Chem., Int. Ed.*, 2022, **61**, 202115219.
- 13 Y. Guo, S. Yao, Y. Xue, X. Hu, H. Cui and Z. Zhou, *Appl. Catal., B*, 2022, **304**, 120997.
- 14 H. Huang, D. Yu, F. Hu, S.-C. Huang, J. Song, H.-Y. Chen, L. L. Li and S. Peng, *Angew. Chem., Int. Ed.*, 2022, **61**, 202116068.
- 15 W. Ma, H. Wan, L. Zhang, J. Y. Zheng and Z. Zhou, *J. Energy Chem.*, 2021, **63**, 170–194.
- 16 T. Zhang, A. G. Walsh, J. Yu and P. Zhang, *Chem. Soc. Rev.*, 2021, **50**, 569–588.
- 17 B. Qiao, A. Wang, X. Yang, L. F. Allard, Z. Jiang, Y. Cui, J. Liu, J. Li and T. Zhang, *Nat. Chem.*, 2011, **3**, 634–641.
- 18 J. Yang, W. H. Li, K. Xu, S. Tan, D. Wang and Y. Li, *Angew. Chem., Int. Ed.*, 2022, **61**, 202200366.
- 19 Z. W. Seh, J. Kibsgaard, C. F. Dickens, I. Chorkendorff, J. K. Nørskov and T. F. Jaramillo, *Science*, 2017, **355**, eaad4998.
- 20 A. Y. Chan, I. B. Perry, N. B. Bissonnette, B. F. Buksh, G. A. Edwards, L. I. Frye, O. L. Garry, M. N. Lavagnino, B. X. Li, Y. Liang, E. Mao, A. Millet, J. V. Oakley, N. L. Reed, H. A. Sakai, C. P. Seath and D. W. C. MacMillan, *Chem. Rev.*, 2022, **122**, 1485–1542.
- 21 Y. Fang, Y. Hou, X. Fu and X. Wang, *Chem. Rev.*, 2022, **122**, 4204–4256.
- 22 L. Jiao, J. Zhu, Y. Zhang, W. Yang, S. Zhou, A. Li, C. Xie, X. Zheng, W. Zhou, S.-H. Yu and H.-L. Jiang, *J. Am. Chem. Soc.*, 2021, **143**, 19417–19424.
- 23 Y. Shi, Z.-R. Ma, Y.-Y. Xiao, Y.-C. Yin, W.-M. Huang, Z.-C. Huang, Y.-Z. Zheng, F.-Y. Mu, R. Huang, G.-Y. Shi, Y.-Y. Sun, X.-H. Xia and W. Chen, *Nat. Commun.*, 2021, **12**, 3021.
- 24 K. L. Zhou, Z. Wang, C. B. Han, X. Ke, C. Wang, Y. Jin, Q. Zhang, J. Liu, H. Wang and H. Yan, *Nat. Commun.*, 2021, **12**, 3783.
- 25 T. Sun, S. Mitchell, J. Li, P. Lyu, X. Wu, J. Perez-Ramirez and J. Lu, *Adv. Mater.*, 2021, **33**, 2003075.
- 26 Y. Liu, B. Wang, Q. Fu, W. Liu, Y. Wang, L. Gu, D. Wang and Y. Li, *Angew. Chem., Int. Ed.*, 2021, **60**, 22522–22528.
- 27 M. Tong, F. Sun, Y. Xie, Y. Wang, Y. Yang, C. Tian, L. Wang and H. Fu, *Angew. Chem., Int. Ed.*, 2021, **60**, 14005–14012.
- 28 L.-S. Zhang, X.-H. Jiang, Z.-A. Zhong, L. Tian, Q. Sun, Y.-T. Cui, X. Lu, J.-P. Zou and S.-L. Luo, *Angew. Chem., Int. Ed.*, 2021, **60**, 21751–21755.
- 29 S. Zhang, X. Ao, J. Huang, B. Wei, Y. Zhai, D. Zhai, W. Deng, C. Su, D. Wang and Y. Li, *Nano Lett.*, 2021, **21**, 9691–9698.
- 30 D. Cao, J. Wang, H. Xu and D. Cheng, *Small*, 2021, **17**, 2101163.
- 31 M. Li, S. Zhao, J. Li, X. Chen, Y. Ji, H. Yu, D. Bai, G. Xu, Z. Zhong and F. Su, *Nano Res.*, 2022, **15**, 5857–5864.
- 32 C. Mochizuki, Y. Inomata, S. Yasumura, M. Lin, A. Taketoshi, T. Honma, N. Sakaguchi, M. Haruta, K.-i. Shimizu, T. Ishida and T. Murayama, *ACS Catal.*, 2022, **12**, 6149–6158.
- 33 S. Si, H. Shou, Y. Mao, X. Bao, G. Zhai, K. Song, Z. Wang, P. Wang, Y. Liu, Z. Zheng, Y. Dai, L. Song, B. Huang and H. Cheng, *Angew. Chem., Int. Ed.*, 2022, **61**, 202209446.
- 34 K. Xiao, R.-T. Lin, J.-X. Wei, N. Li, H. Li, T. Ma and Z.-Q. Liu, *Nano Res.*, 2022, **15**, 4980–4985.
- 35 L. Sun, L. R. Cao, Y. Su, C. J. Wang, J. Lin and X. D. Wang, *Appl. Catal., B*, 2022, **318**, 121841.
- 36 G. D. Ding, L. D. Hao, H. P. Xu, L. G. Wang, J. Chen, T. Li, X. M. Tu and Q. Zhang, *Chem. Commun.*, 2020, **3**, 43.
- 37 W. Liu, F. Morfin, K. Provost, M. Bahri, W. Baaziz, O. Ersen, L. Piccolo and C. Zlotea, *Nanoscale*, 2022, **14**, 7641–7649.
- 38 Q. Shen, H. Jin, P. Li, X. Yu, L. Zheng, W. Song and C. Cao, *Nano Res.*, 2022, **15**, 5024–5031.

- 39 A. R. Poerwoprajitno, L. Gloag, J. Watt, S. Cheong, X. Tan, H. Lei, H. A. Tahini, A. Henson, B. Subhash, N. M. Bedford, B. K. Miller, P. B. O'Mara, T. M. Benedetti, D. L. Huber, W. Zhang, S. C. Smith, J. J. Gooding, W. Schuhmann and R. D. Tilley, *Nat. Catal.*, 2022, **5**, 231–237.
- 40 L. Wang, L. Zhang, W. Ma, H. Wan, X. Zhang, X. Zhang, S. Jiang, J. Y. Zheng and Z. Zhou, *Adv. Funct. Mater.*, 2022, **32**, 2203342.
- 41 Z. Li, W. Wei, H. Li, S. Li, L. Leng, M. Zhang, J. H. Horton, D. Wang, W. Sun, C. Guo, W. Wu and J. Wang, *ACS Nano*, 2021, **15**, 10175–10184.
- 42 Z. Sun, Y. Yang, C. Fang, Y. Yao, F. Qin, H. Gu, Q. Liu, W. Xu, H. Tang, Z. Jiang, B. Ge, W. Chen and Z. Chen, *Small*, 2022, **18**, 2203422.
- 43 S. Jiao, M. Kong, Z. Hu, S. Zhou, X. Xu and L. Liu, *Small*, 2022, **18**, 2105129.
- 44 F. Kong, X. Liu, Y. Song, Z. Qian, J. Li, L. Zhang, G. Yin, J. Wang, D. Su and X. Sun, *Angew. Chem., Int. Ed.*, 2022, **61**, 202207524.
- 45 L. Zhang, Q. Wang, L. Li, M. N. Banis, J. Li, K. Adair, Y. Sun, R. Li, Z.-J. Zhao, M. Gu and X. Sun, *Nano Energy*, 2022, **93**, 106813.
- 46 J. Liu, C. Cao, X. Liu, L. Zheng, X. Yu, Q. Zhang, L. Gu, R. Qi and W. Song, *Angew. Chem., Int. Ed.*, 2021, **60**, 15248–15253.
- 47 J. Yang, J. Zhang, Q. Jiang, Y. Su, Y. Cui, X. Li, S. Zhang, W. Li and B. Qiao, *J. Chem. Phys.*, 2021, **154**, 131105.
- 48 J. Leverett, J. A. Yuwono, P. Kumar, T. Tran-Phu, J. Qu, J. Cairney, X. Wang, A. N. Simonov, R. K. Hocking, B. Johannessen, L. Dai, R. Daiyan and R. Amal, *ACS Energy Lett.*, 2022, **7**, 920–928.
- 49 J. Shi, Y. Wei, D. Zhou, L. Zhang, X. Yang, Z. Miao, H. Qi, S. Zhang, A. Li, X. Liu, W. Yan, Z. Jiang, A. Wang and T. Zhang, *ACS Catal.*, 2022, **12**, 7760–7772.
- 50 Y. Chen, S. Ji, C. Chen, Q. Peng, D. Wang and Y. Li, *Joule*, 2018, **2**, 1242–1264.
- 51 K. Qi, M. Chhowalla and D. Voiry, *Mater. Today*, 2020, **40**, 173–192.
- 52 K. Wu, K. Sun, S. Liu, W.-C. Cheong, Z. Chen, C. Zhang, Y. Pan, Y. Cheng, Z. Zhuang, X. Wei, Y. Wang, L. Zheng, Q. Zhang, D. Wang, Q. Peng, C. Chen and Y. Li, *Nano Energy*, 2021, **80**, 105467.
- 53 K. Jiang, M. Luo, Z. Liu, M. Peng, D. Chen, Y.-R. Lu, T.-S. Chan, F. M. F. de Groot and Y. Tan, *Nat. Commun.*, 2021, **12**, 1687.
- 54 C. Xia, Y. Qiu, Y. Xia, P. Zhu, G. King, X. Zhang, Z. Wu, J. Y. Kim, D. A. Cullen, D. Zheng, P. Li, M. Shakouri, E. Heredia, P. Cui, H. N. Alshareef, Y. Hu and H. Wang, *Nat. Chem.*, 2021, **13**, 887.
- 55 J. Yang, W. Li, D. Wang and Y. Li, *Adv. Mater.*, 2020, **32**, 2003300.
- 56 H. Jin, P. Li, P. Cui, J. Shi, W. Zhou, X. Yu, W. Song and C. Cao, *Nat. Commun.*, 2022, **13**, 723.
- 57 T. Zhang, A. G. Walsh, J. Yu and P. Zhang, *Chem. Soc. Rev.*, 2021, **50**, 569–588.
- 58 H. Peng, T. Yang, H. Lin, Y. Xu, Z. Wang, Q. Zhang, S. Liu, H. Geng, L. Gu, C. Wang, X. Fan, W. Chen and X. Huang, *Adv. Energy Mater.*, 2022, **12**, 2201668.
- 59 M. Wu, G. Zhang, W. Wang, H. Yang, D. Rawach, M. Chen and S. Sun, *Small Methods*, 2022, **6**, 2100947.
- 60 M. Gao, F. Tian, Z. Guo, X. Zhang, Z. Li, J. Zhou, X. Zhou, Y. Yu and W. Yang, *Chem. Eng. J.*, 2022, **446**, 137127.
- 61 J. Xu, H. Xu, A. Dong, H. Zhang, Y. Zhou, H. Dong, B. Tang, Y. Liu, L. Zhang, X. Liu, J. Luo, L. Bie, S. Dai, Y. Wang, X. Sun and Y. Li, *Adv. Mater.*, 2022, **34**, 2206991.
- 62 W. Ma, R. Ma, C. Wang, J. Liang, X. Liu, K. Zhou and T. Sasaki, *ACS Nano*, 2015, **9**, 1977–1984.
- 63 G. Chen, H. Wan, W. Ma, N. Zhang, Y. Cao, X. Liu, J. Wang and R. Ma, *Adv. Energy Mater.*, 2020, **10**, 1902535.
- 64 H. Wan, X. Xiao, W. Ma, Y. Zhang, X. Liu, Y. Liu, G. Chen, N. Zhang, Y. Cao and R. Ma, *Inorg. Chem. Front.*, 2022, **9**, 83–89.
- 65 J. Zhang, J. Ma, T. S. Choksi, D. Zhou, S. Han, Y. F. Liao, H. B. Yang, D. Liu, Z. Zeng, W. Liu, X. Sun, T. Zhang and B. Liu, *J. Am. Chem. Soc.*, 2022, **144**, 2255–2263.
- 66 X. Sun, Y. Tuo, C. Ye, C. Chen, Q. Lu, G. Li, P. Jiang, S. Chen, P. Zhu, M. Ma, J. Zhang, J. H. Bitter, D. Wang and Y. Li, *Angew. Chem., Int. Ed.*, 2021, **60**, 23614–23618.
- 67 J. Yang, W.-H. Li, K. Xu, S. Tan, D. Wang and Y. Li, *Angew. Chem., Int. Ed.*, 2022, **61**, 202200366.
- 68 L. Gong, D. Zhang, C.-Y. Lin, Y. Zhu, Y. Shen, J. Zhang, X. Han, L. Zhang and Z. Xia, *Adv. Energy Mater.*, 2019, **9**, 1902625.
- 69 Z. Zhang, J. Zhu, S. Chen, W. Sun and D. Wang, *Angew. Chem., Int. Ed.*, 2023, **62**, 202215136.
- 70 J. Li, Q. Guan, H. Wu, W. Liu, Y. Lin, Z. Sun, X. Ye, X. Zheng, H. Pan, J. Zhu, S. Chen, W. Zhang, S. Wei and J. Lu, *J. Am. Chem. Soc.*, 2019, **141**, 14515–14519.
- 71 X. Duan, P. Li, D. Zhou, S. Wang, H. Liu, Z. Wang, X. Zhang, G. Yang, Z. Zhang, G. Tan, Y. Li, L. Xu, W. Liu, Z. Xing, Y. Kuang and X. Sun, *Chem. Eng. J.*, 2022, **446**, 136962.
- 72 G. Han, X. Zhang, W. Liu, Q. Zhang, Z. Wang, J. Cheng, T. Yao, L. Gu, C. Du, Y. Gao and G. Yin, *Nat. Commun.*, 2021, **12**, 6335.
- 73 J. Zhang, G. Zeng, L. Chen, W. Lai, Y. Yuan, Y. Lu, C. Ma, W. Zhang and H. Huang, *Nano Res.*, 2022, **15**, 4014–4022.
- 74 S.-N. Zhao, J.-K. Li, R. Wang, J. Cai and S.-Q. Zang, *Adv. Mater.*, 2022, **34**, 2107291.
- 75 H. Cai, G. Zhang, X. Zhang, B. Chen, Z. Lu, H. Xu, R. Gao and C. Shi, *Small*, 2022, **18**, 2200911.
- 76 X. Wang, Y. Zhang, J. Wu, Z. Zhang, Q. Liao, Z. Kang and Y. Zhang, *Chem. Rev.*, 2022, **122**, 1273–1348.
- 77 Y. Wang, X. Li, M. Zhang, J. Zhang, Z. Chen, X. Zheng, Z. Tian, N. Zhao, X. Han, K. Zaghbi, Y. Wang, Y. Deng and W. Hu, *Adv. Mater.*, 2022, **34**, 2107053.
- 78 L. Cao, X. Liu, X. Shen, D. Wu and T. Yao, *Acc. Chem. Res.*, 2022, **55**, 2594–2603.
- 79 W. Q. Zheng, R. Zhu, H. J. Wu, T. Ma, H. J. Zhou, M. Zhou, C. He, X. K. Liu, S. Li and C. Cheng, *Angew. Chem., Int. Ed.*, 2022, **61**, 202208667.

- 80 C.-X. Zhao, J.-N. Liu, J. Wang, C. Wang, X. Guo, X.-Y. Li, X. Chen, L. Song, B.-Q. Li and Q. Zhang, *Sci. Adv.*, 2022, **8**, eabn5091.
- 81 X. Liu, Y. Deng, L. Zheng, M. R. Kesama, C. Tang and Y. Zhu, *ACS Catal.*, 2022, **12**, 5517–5526.
- 82 Y. Chen, J. Lin, B. Jia, X. Wang, S. Jiang and T. Ma, *Adv. Mater.*, 2022, **34**, 2201796.
- 83 Y. Liu, X. Liu, A. R. Jadhav, T. Yang, Y. Hwang, H. Wang, L. Wang, Y. Luo, A. Kumar, J. Lee, H. T. D. Bui, M. G. Kim and H. Lee, *Angew. Chem., Int. Ed.*, 2022, **61**, 202114160.
- 84 Y. Cheng, H. Guo, X. Li, X. Wu, X. Xu, L. Zheng and R. Song, *Chem. Eng. J.*, 2021, **410**, 128359.
- 85 J. Huo, Z. Shen, X. Cao, L. Li, Y. Zhao, H. Liu and G. Wang, *Small*, 2022, **18**, 2202394.
- 86 Y. Wu, Q. Wu, Q. Zhang, Z. Lou, K. Liu, Y. Ma, Z. Wang, Z. Zheng, H. Cheng, Y. Liu, Y. Dai, B. Huang and P. Wang, *Energy Environ. Sci.*, 2022, **15**, 1271–1281.
- 87 X. I. Percira-Hernandez, A. DeLaRiva, V. Muravev, D. Kunwar, H. Xiong, B. Sudduth, M. Engelhard, L. Kovarik, E. J. M. Hensen, Y. Wang and A. K. Datye, *Nat. Commun.*, 2019, **10**, 1358.
- 88 R. Santhosh Kumar, S. Ramakrishnan, S. Prabhakaran, A. R. Kim, D. R. Kumar, D. H. Kim and D. J. Yoo, *J. Mater. Chem. A*, 2022, **10**, 1999–2011.
- 89 N. Logeshwaran, S. Ramakrishnan, S. S. Chandrasekaran, M. Vinothkannan, A. R. Kim, S. Sengodan, D. B. Velusamy, P. Varadhan, J.-H. He and D. J. Yoo, *Appl. Catal., B*, 2021, **297**, 120405.
- 90 W. Liu, H. Zhang, C. Li, X. Wang, J. Liu and X. Zhang, *J. Energy Chem.*, 2020, **47**, 333–345.
- 91 S. Tian, B. Wang, W. Gong, Z. He, Q. Xu, W. Chen, Q. Zhang, Y. Zhu, J. Yang, Q. Fu, C. Chen, Y. Bu, L. Gu, X. Sun, H. Zhao, D. Wang and Y. Li, *Nat. Commun.*, 2021, **12**, 3181.
- 92 S. C. Karthikeyan, R. Santhosh Kumar, S. Ramakrishnan, S. Prabhakaran, A. R. Kim, D. H. Kim and D. J. Yoo, *ACS Sustainable Chem. Eng.*, 2022, **10**, 15068–15081.
- 93 R. Santhosh Kumar, S. C. Karthikeyan, S. Ramakrishnan, S. Vijayapradeep, A. Rhan Kim, J.-S. Kim and D. Jin Yoo, *Chem. Eng. J.*, 2023, **451**, 138471.
- 94 L. Sun, L. Cao, Y. Su, C. Wang, J. Lin and X. Wang, *Appl. Catal., B*, 2022, **318**, 121841.
- 95 J. Fonseca and J. Lu, *ACS Catal.*, 2021, **11**, 7018–7059.
- 96 S. Jiao, M. Kong, Z. Hu, S. Zhou, X. Xu and L. Liu, *Small*, 2022, **18**, 2105129.
- 97 R. Ramesh, S. Han, D. K. Nandi, S. Y. Sawant, D. H. Kim, T. Cheon, M. H. Cho, R. Harada, T. Shigetomi, K. Suzuki and S.-H. Kim, *Adv. Mater. Interfaces*, 2021, **8**, 2001508.
- 98 Y. Li, S. L. Zhang, W. Cheng, Y. Chen, D. Luan, S. Gao and X. W. D. Lou, *Adv. Mater.*, 2022, **34**, 2105204.
- 99 T. Al-Zoubi, Y. Zhou, X. Yin, B. Janicek, C. Sun, C. E. Schulz, X. Zhang, A. A. Gewirth, P. Huang, P. Zelenay and H. Yang, *J. Am. Chem. Soc.*, 2020, **142**, 5477–5481.
- 100 H. Wei, K. Huang, L. Zhang, B. Ge, D. Wang, J. Lang, J. Ma, D. Wang, S. Zhang, Q. Li, R. Zhang, N. Hussain, M. Lei, L.-M. Liu and H. Wu, *Angew. Chem., Int. Ed.*, 2018, **57**, 3354–3359.
- 101 H. Wei, K. Huang, D. Wang, R. Zhang, B. Ge, J. Ma, B. Wen, S. Zhang, Q. Li, M. Lei, C. Zhang, J. Irawan, L. M. Liu and H. Wu, *Nat. Commun.*, 2017, **8**, 1490.
- 102 G.-F. Han, F. Li, A. I. Rykov, Y.-K. Im, S.-Y. Yu, J.-P. Jeon, S.-J. Kim, W. Zhou, R. Ge, Z. Ao, T. J. Shin, J. Wang, H. Y. Jeong and J.-B. Baek, *Nat. Nanotechnol.*, 2022, **17**, 403–407.
- 103 H. Fei, J. Dong, C. Wan, Z. Zhao, X. Xu, Z. Lin, Y. Wang, H. Liu, K. Zang, J. Luo, S. Zhao, W. Hu, W. Yan, I. Shakir, Y. Huang and X. Duan, *Adv. Mater.*, 2018, **30**, 1802146.
- 104 Z. Zhang, C. Feng, C. Liu, M. Zuo, L. Qin, X. Yan, Y. Xing, H. Li, R. Si, S. Zhou and J. Zeng, *Nat. Commun.*, 2020, **11**, 1215.
- 105 V. Muravev, G. Spezzati, Y.-Q. Su, A. Parastaev, F.-K. Chiang, A. Longo, C. Escudero, N. Kosinov and E. J. M. Hensen, *Nat. Catal.*, 2021, **4**, 469–478.
- 106 X. Wu, H. Zhang, S. Zuo, J. Dong, Y. Li, J. Zhang and Y. Han, *Nano-Micro Lett.*, 2021, **13**, 136.
- 107 A. R. Poerwoprajitno, L. Gloag, J. Watt, S. Cheong, X. Tan, H. Lei, H. A. Tahini, A. Henson, B. Subhash, N. M. Bedford, B. K. Miller, P. B. O'Mara, T. M. Benedetti, D. L. Huber, W. Zhang, S. C. Smith, J. J. Gooding, W. Schuhmann and R. D. Tilley, *Nat. Catal.*, 2022, **5**, 231–237.
- 108 L. DeRita, J. Resasco, S. Dai, A. Boubnov, H. V. Thang, A. S. Hoffman, I. Ro, G. W. Graham, S. R. Bare, G. Pacchioni, X. Pan and P. Christopher, *Nat. Mater.*, 2019, **18**, 746–751.
- 109 S. Mühlenberend, M. Gruyters and R. Berndt, *Phys. Rev. B: Condens. Matter Mater. Phys.*, 2013, **88**, 115301.
- 110 Z. Zhu, H. Yin, Y. Wang, C. H. Chuang, L. Xing, M. Dong, Y. R. Lu, G. Casillas-Garcia, Y. Zheng, S. Chen, Y. Dou, P. Liu, Q. Cheng and H. Zhao, *Adv. Mater.*, 2020, **32**, 2004670.
- 111 L. Zeng, Z. Zhao, F. Lv, Z. Xia, S. Y. Lu, J. Li, K. Sun, K. Wang, Y. Sun, Q. Huang, Y. Chen, Q. Zhang, L. Gu, G. Lu and S. Guo, *Nat. Commun.*, 2022, **13**, 3822.
- 112 M. M. J. Treacy, A. Howie and C. J. Wilson, *Philos. Mag.*, 1978, **32**, 569–585.
- 113 S. Hejazi, S. Mohajernia, B. Osuagwu, G. Zoppellaro, P. Andryskova, O. Tomanec, S. Kment, R. Zboril and P. Schmuki, *Adv. Mater.*, 2020, **32**, 1908505.
- 114 S. Liang, Q. Jiang, Q. Wang and Y. Liu, *Adv. Energy Mater.*, 2021, **11**, 2101477.
- 115 W. Yang, P. Cheng, Z. Li, Y. Lin, M. Li, J. Zi, H. Shi, G. Li, Z. Lian and H. Li, *Adv. Funct. Mater.*, 2022, **32**, 2205920.
- 116 C. J. Chen, *Phys. Rev. Lett.*, 1990, **65**, 448–451.
- 117 T. Zhang, Z. Chen, A. G. Walsh, Y. Li and P. Zhang, *Adv. Mater.*, 2020, **32**, 2002910.
- 118 D. Bagchi, N. Phukan, S. Sarkar, R. Das, B. Ray, P. Bellare, N. Ravishankar and S. C. Peter, *J. Mater. Chem. A*, 2021, **9**, 9319–9326.
- 119 K. Jiang, S. Siahrostami, T. Zheng, Y. Hu, S. Hwang, E. Stavitski, Y. Peng, J. Dynes, M. Gangisetty, D. Su, K. Attenkofer and H. Wang, *Energy Environ. Sci.*, 2018, **11**, 893–903.

- 120 C. Yang, Z. Miao, F. Zhang, L. Li, Y. Liu, A. Wang and T. Zhang, *Green Chem.*, 2018, **20**, 2142–2150.
- 121 D. Bagchi, S. Sarkar, A. K. Singh, C. P. Vinod and S. C. Peter, *ACS Nano*, 2022, **16**, 6158–6196.
- 122 W. Zhang, C. Huang, J. Zhu, Q. Zhou, R. Yu, Y. Wang, P. An, J. Zhang, M. Qiu, L. Zhou, L. Mai, Z. Yi and Y. Yu, *Angew. Chem., Int. Ed.*, 2022, **61**, 202112116.
- 123 S. Inoue, T. Nakajima and Y. Kikuchi, *Carbon*, 2006, **44**, 1287–1291.
- 124 J.-H. Zhong, X. Jin, L. Meng, X. Wang, H.-S. Su, Z.-L. Yang, C. T. Williams and B. Ren, *Nat. Nanotechnol.*, 2017, **12**, 132–136.
- 125 J. Chen, G. Liu, Y.-z. Zhu, M. Su, P. Yin, X.-j. Wu, Q. Lu, C. Tan, M. Zhao, Z. Liu, W. Yang, H. Li, G.-H. Nam, L. Zhang, Z. Chen, X. Huang, P. M. Radjenovic, W. Huang, Z.-q. Tian, J.-f. Li and H. Zhang, *J. Am. Chem. Soc.*, 2020, **142**, 7161–7167.
- 126 G. Shi, Y. Xie, L. Du, X. Fu, X. Chen, W. Xie, T.-B. Lu, M. Yuan and M. Wang, *Angew. Chem., Int. Ed.*, 2022, **61**, 202203569.
- 127 J. Wei, S. N. Qin, J. Yang, H. L. Ya, W. H. Huang, H. Zhang, B. J. Hwang, Z. Q. Tian and J. F. Li, *Angew. Chem., Int. Ed.*, 2021, **60**, 9306–9310.
- 128 B. Hu, K. Sun, Z. Zhuang, Z. Chen, S. Liu, W.-C. Cheong, C. Chen, M. Hu, X. Cao, J. Ma, R. Tu, X. Zheng, H. Xiao, X. Chen, Y. Cui, Q. Peng, C. Chen and Y. Li, *Adv. Mater.*, 2022, **34**, 2107721.
- 129 R. Ge, Y. Wang, Z. Li, M. Xu, S. M. Xu, H. Zhou, K. Ji, F. Chen, J. Zhou and H. Duan, *Angew. Chem., Int. Ed.*, 2022, **61**, 202200211.
- 130 H. Ali-Löytty, M. W. Louie, M. R. Singh, L. Li, H. G. Sanchez Casalongue, H. Ogasawara, E. J. Crumlin, Z. Liu, A. T. Bell, A. Nilsson and D. Friebe, *J. Phys. Chem. C*, 2016, **120**, 2247–2253.
- 131 L. Wang, X. Li, X. Hu, S. Chen, Z. Qiu, Y. Wang, H. Zhang, Y. Yu, B. Yang, Y. Yang, P. Orgiani, C. Aruta and N. Yang, *Nano Res.*, 2023, **16**, 3278–3286.
- 132 L. Nguyen, F. F. Tao, Y. Tang, J. Dou and X. J. Bao, *Chem. Rev.*, 2019, **119**, 6822–6905.
- 133 L. Chen, Y. Tian, X. Hu, S. Yao, Z. Lu, S. Chen, X. Zhang and Z. Zhou, *Adv. Funct. Mater.*, 2022, **32**, 2208418.
- 134 X. Hu, S. Chen, L. Chen, Y. Tian, S. Yao, Z. Lu, X. Zhang and Z. Zhou, *J. Am. Chem. Soc.*, 2022, **144**, 18144–18152.
- 135 X. Zhao, Z. H. Levell, S. Yu and Y. Liu, *Chem. Rev.*, 2022, **122**, 10675–10709.
- 136 X. Zhao and Y. Liu, *J. Am. Chem. Soc.*, 2020, **142**, 5773–5777.
- 137 X. Hu, S. Yao, L. Chen, X. Zhang, M. Jiao, Z. Lu and Z. Zhou, *J. Mater. Chem. A*, 2021, **9**, 23515–23521.
- 138 R. Zhang, L. Jiao, W. Yang, G. Wan and H.-L. Jiang, *J. Mater. Chem. A*, 2019, **7**, 26371–26377.
- 139 X. Liu, Y. Jiao, Y. Zheng, M. Jaroniec and S. Z. Qiao, *J. Am. Chem. Soc.*, 2019, **141**, 9664–9672.
- 140 X. Zheng, J. Tang, A. Gallo, J. A. Garrido Torres, X. Yu, C. J. Athanitis, E. M. Been, P. Ercius, H. Mao, S. C. Fakra, C. Song, R. C. Davis, J. A. Reimer, J. Vinson, M. Bajdich and Y. Cui, *Proc. Natl. Acad. Sci. U. S. A.*, 2021, **118**, 2101817118.
- 141 H. Jeong, D. Shin, B. S. Kim, J. Bae, S. Shin, C. Choe, J. W. Han and H. Lee, *Angew. Chem., Int. Ed.*, 2020, **59**, 20691–20696.
- 142 D. Cao, H. Xu, H. Li, C. Feng, J. Zeng and D. Cheng, *Nat. Commun.*, 2022, **13**, 5843.
- 143 C. Wan, X. Duan and Y. Huang, *Adv. Energy Mater.*, 2020, **10**, 1903815.
- 144 X. F. Lu, B. Y. Xia, S.-Q. Zang and X. W. Lou, *Angew. Chem., Int. Ed.*, 2020, **59**, 4634–4650.
- 145 Z. Jin, P. Li, Y. Meng, Z. Fang, D. Xiao and G. Yu, *Nat. Catal.*, 2021, **4**, 615–622.
- 146 F. Luo, A. Roy, L. Silvioli, D. A. Cullen, A. Zitolo, M. T. Sougrati, I. C. Oguz, T. Mineva, D. Teschner, S. Wagner, J. Wen, F. Dionigi, U. I. Kramm, J. Rossmeisl, F. Jaouen and P. Strasser, *Nat. Mater.*, 2020, **19**, 1215–1223.
- 147 J. Yang, Z. Wang, C. X. Huang, Y. Zhang, Q. Zhang, C. Chen, J. Du, X. Zhou, Y. Zhang, H. Zhou, L. Wang, X. Zheng, L. Gu, L. M. Yang and Y. Wu, *Angew. Chem., Int. Ed.*, 2021, **60**, 22722–22728.
- 148 Y. Xie, J. Cai, Y. Wu, Y. Zang, X. Zheng, J. Ye, P. Cui, S. Niu, Y. Liu, J. Zhu, X. Liu, G. Wang and Y. Qian, *Adv. Mater.*, 2019, **31**, 1807780.
- 149 R. Wan, M. Luo, J. Wen, S. Liu, X. Kang and Y. Tian, *J. Energy Chem.*, 2022, **69**, 44–53.
- 150 M. Li, S. Wang, X. Wang, X. Tian, X. Wu, Y. Zhou, G. Hu and L. Feng, *Chem. Eng. J.*, 2022, **442**, 136165.
- 151 F. Dionigi, J. Zhu, Z. Zeng, T. Merzdorf, H. Sarodnik, M. Gliech, L. Pan, W.-X. Li, J. Greeley and P. Strasser, *Angew. Chem., Int. Ed.*, 2021, **60**, 14446–14457.
- 152 Y. Wu, Y. Zhao, P. Zhai, C. Wang, J. Gao, L. Sun and J. Hou, *Adv. Mater.*, 2022, **34**, 2202523.
- 153 N. Zhang and Y. Chai, *Energy Environ. Sci.*, 2021, **14**, 4647–4671.
- 154 Z. Sun, L. Lin, J. He, D. Ding, T. Wang, J. Li, M. Li, Y. Liu, Y. Li, M. Yuan, B. Huang, H. Li and G. Sun, *J. Am. Chem. Soc.*, 2022, **144**, 8204–8213.
- 155 Y. Sun, J. Wang, Q. Liu, M. Xia, Y. Tang, F. Gao, Y. Hou, J. Tse and Y. Zhao, *J. Mater. Chem. A*, 2019, **7**, 27175–27185.
- 156 X. Wei, S. Song, W. Cai, X. Luo, L. Jiao, Q. Fang, X. Wang, N. Wu, Z. Luo, H. Wang, Z. Zhu, J. Li, L. Zheng, W. Gu, W. Song, S. Guo and C. Zhu, *Chem*, 2022, **8**, 2136–2147.
- 157 T. Wang, A. Chutia, D. J. L. Brett, P. R. Shearing, G. He, G. Chai and I. P. Parkin, *Energy Environ. Sci.*, 2021, **14**, 2639–2669.
- 158 X. Ao, W. Zhang, B. Zhao, Y. Ding, G. Nam, L. Soule, A. Abdelhafiz, C. Wang and M. Liu, *Energy Environ. Sci.*, 2020, **13**, 3032–3040.
- 159 X. Wei, X. Luo, N. Wu, W. Gu, Y. Lin and C. Zhu, *Nano Energy*, 2021, **84**, 105817.
- 160 C. Wan, X. Duan and Y. Huang, *Adv. Energy Mater.*, 2020, **10**, 1903815.
- 161 M. Tong, F. Sun, Y. Xie, Y. Wang, Y. Yang, C. Tian, L. Wang and H. Fu, *Angew. Chem., Int. Ed.*, 2021, **60**, 14005–14012.
- 162 Z. Chen, X. Zhang, W. Liu, M. Jiao, K. Mou, X. Zhang and L. Liu, *Energy Environ. Sci.*, 2021, **14**, 2349–2356.
- 163 T. Tang, Z. Wang and J. Guan, *Adv. Funct. Mater.*, 2022, **32**, 2111504.

- 164 S. Ren, D. Joulié, D. Salvatore, K. Torbensen, M. Wang, M. Robert and C. P. Berlinguette, *Science*, 2019, **365**, 367–369.
- 165 M. W. Jia, C. Choi, T. S. Wu, C. Ma, P. Kang, H. C. Tao, Q. Fan, S. Hong, S. Z. Liu, Y. L. Soo, Y. S. Jung, J. S. Qiu and Z. Y. Sun, *Chem. Sci.*, 2018, **9**, 8775–8780.
- 166 S. Li, S. Zhao, X. Lu, M. Ceccato, X. M. Hu, A. Roldan, J. Catalano, M. Liu, T. Skrydstrup and K. Daasbjerg, *Angew. Chem., Int. Ed.*, 2021, **60**, 22826–22832.
- 167 D. Fang, P. Sun, S. Huang, Y. Shang, X. Li, D. Yan, Y. V. Lim, C.-Y. Su, B.-J. Su, J.-Y. Juang and H. Y. Yang, *ACS Mater. Lett.*, 2022, **4**, 1–10.
- 168 X. Liang, D. Wang, Z. Zhao, T. Li, Y. Gao and C. Hu, *Adv. Funct. Mater.*, 2022, **32**, 2203001.
- 169 J. R. Huang, X. F. Qiu, Z. H. Zhao, H. L. Zhu, Y. C. Liu, W. Shi, P. Q. Liao and X. M. Chen, *Angew. Chem., Int. Ed.*, 2022, **61**, 202210985.
- 170 Y. Guo, S. Yao, Y. Xue, X. Hu, H. Cui and Z. Zhou, *Appl. Catal., B*, 2022, **304**, 120997.
- 171 P. Kuang, Y. Wang, B. Zhu, F. Xia, C. W. Tung, J. Wu, H. M. Chen and J. Yu, *Adv. Mater.*, 2021, **33**, 2008599.
- 172 P. Sun, Z. Qiao, S. Wang, D. Li, X. Liu, Q. Zhang, L. Zheng, Z. Zhuang and D. Cao, *Angew. Chem., Int. Ed.*, 2023, **62**, 202216041.
- 173 X. Long, Z. Li, G. Gao, P. Sun, J. Wang, B. Zhang, J. Zhong, Z. Jiang and F. Li, *Nat. Commun.*, 2020, **11**, 4074.
- 174 S. Zhang, M. Jin, T. Shi, M. Han, Q. Sun, Y. Lin, Z. Ding, L. R. Zheng, G. Wang, Y. Zhang, H. Zhang and H. Zhao, *Angew. Chem., Int. Ed.*, 2020, **59**, 13423–13429.
- 175 X. Sun, Y. Tuo, C. Ye, C. Chen, Q. Lu, G. Li, P. Jiang, S. Chen, P. Zhu, M. Ma, J. Zhang, J. H. Bitter, D. Wang and Y. Li, *Angew. Chem., Int. Ed.*, 2021, **60**, 23614–23618.
- 176 F. Pan, B. Li, E. Sarnello, S. Hwang, Y. Gang, X. Feng, X. Xiang, N. M. Adli, T. Li, D. Su, G. Wu, G. Wang and Y. Li, *Nano Energy*, 2020, **68**, 104384.
- 177 S. Ji, B. Jiang, H. Hao, Y. Chen, J. Dong, Y. Mao, Z. Zhang, R. Gao, W. Chen, R. Zhang, Q. Liang, H. Li, S. Liu, Y. Wang, Q. Zhang, L. Gu, D. Duan, M. Liang, D. Wang, X. Yan and Y. Li, *Nat. Catal.*, 2021, **4**, 407–417.
- 178 K. Li, S. Zhang, X. Zhang, S. Liu, H. Jiang, T. Jiang, C. Shen, Y. Yu and W. Chen, *Nano Lett.*, 2022, **22**, 1557–1565.
- 179 H. B. Yang, S.-F. Hung, S. Liu, K. Yuan, S. Miao, L. Zhang, X. Huang, H.-Y. Wang, W. Cai, R. Chen, J. Gao, X. Yang, W. Chen, Y. Huang, H. M. Chen, C. M. Li, T. Zhang and B. Liu, *Nat. Energy*, 2018, **3**, 140–147.
- 180 Y. Wang, Y.-J. Tang and K. Zhou, *J. Am. Chem. Soc.*, 2019, **141**, 14115–14119.
- 181 J.-X. Peng, W. Yang, Z. Jia, L. Jiao and H.-L. Jiang, *Nano Res.*, 2022, **15**, 10063–10069.
- 182 Y. Liu, S. Zhang, C. Jiao, H. Chen, G. Wang, W. Wu, Z. Zhuo and J. Mao, *Adv. Sci.*, 2023, **10**, 2206107.
- 183 K.-M. Zhao, S. Liu, Y.-Y. Li, X. Wei, G. Ye, W. Zhu, Y. Su, J. Wang, H. Liu, Z. He, Z.-Y. Zhou and S.-G. Sun, *Adv. Energy Mater.*, 2022, **12**, 2103588.
- 184 X. Li, C.-S. Cao, S.-F. Hung, Y.-R. Lu, W. Cai, A. I. Rykov, S. Miao, S. Xi, H. Yang, Z. Hu, J. Wang, J. Zhao, E. E. Alp, W. Xu, T.-S. Chan, H. Chen, Q. Xiong, H. Xiao, Y. Huang, J. Li, T. Zhang and B. Liu, *Chem*, 2020, **6**, 3440–3454.
- 185 Z. Chen, A. Huang, K. Yu, T. Cui, Z. Zhuang, S. Liu, J. Li, R. Tu, K. Sun, X. Tan, J. Zhang, D. Liu, Y. Zhang, P. Jiang, Y. Pan, C. Chen, Q. Peng and Y. Li, *Energy Environ. Sci.*, 2021, **14**, 3430–3437.
- 186 Y. Shi, Z. R. Ma, Y. Y. Xiao, Y. C. Yin, W. M. Huang, Z. C. Huang, Y. Z. Zheng, F. Y. Mu, R. Huang, G. Y. Shi, Y. Y. Sun, X. H. Xia and W. Chen, *Nat. Commun.*, 2021, **12**, 3021.
- 187 C. Tsounis, B. Subhash, P. V. Kumar, N. M. Bedford, Y. Zhao, J. Shenoy, Z. Ma, D. Zhang, C. Y. Toe, S. Cheong, R. D. Tilley, X. Lu, L. Dai, Z. Han and R. Amal, *Adv. Funct. Mater.*, 2022, **32**, 2203067.
- 188 X. Zheng, J. Tang, A. Gallo, J. A. Garrido Torres, X. Yu, C. J. Athanitis, E. M. Been, P. Ercius, H. Mao, S. C. Fakra, C. Song, R. C. Davis, J. A. Reimer, J. Vinson, M. Bajdich and Y. Cui, *Proc. Natl. Acad. Sci. U. S. A.*, 2021, **118**, 2101817118.
- 189 Z. Li, B. Li, Y. Hu, S. Wang and C. Yu, *Materials Advances*, 2022, **3**, 779–809.
- 190 P. Zhai, M. Xia, Y. Wu, G. Zhang, J. Gao, B. Zhang, S. Cao, Y. Zhang, Z. Li, Z. Fan, C. Wang, X. Zhang, J. T. Miller, L. Sun and J. Hou, *Nat. Commun.*, 2021, **12**, 4587.
- 191 X. Duan, P. Li, D. Zhou, S. Wang, H. Liu, Z. Wang, X. Zhang, G. Yang, Z. Zhang, G. Tan, Y. Li, L. Xu, W. Liu, Z. Xing, Y. Kuang and X. Sun, *Chem. Eng. J.*, 2022, **446**, 136962.